The SPIRE Analogue Signal Chain and Photometer Detector Data Processing Pipeline

Document Number: SPIRE-UCF-DOC-002890

Matt Griffin

Issue 5
1 August 2008

Changes and additions with respect to Issue 4 (20 Feb. 2008) are in blue text

Contents

1. Introduction

The purpose of this note is to describe the propagation of the SPIRE science data signals from the detectors through to the digitised samples transmitted to the ground, and to outline the methods by which the measured detector voltages are to be converted to astronomical signals.

Section 2 contains a list of the symbols used in the document.

Section 3 describes the analogue signal chains for both the photometer and FTS, and is largely based on information in the *DCU Design Document* (*DCU DD*) [1]. It concludes with a description of how the Photometer and Spectrometer Data Timeline (PDT and SDT) products (bolometer voltage and resistance) are to be derived from the telemetry data. This section applies both to the photometer and FTS pipelines, the only differences being in the values of various parameters and in the form of some of the transfer functions. Subsequent stages of the two pipelines will have some common features, but will be different in many respects. The FTS pipeline following the derivation of the Spectrometer Detector Timeline (SDT) products is described in detail in [2].

Section 4 deals with the transient response of the photometer signal chain, taking into account the characteristics of the detectors and the analogue filter, and the observing modes.

The SPIRE observing modes are described in *Operating Modes for the SPIRE Instrument* [3]. The photometer pipelines (one for scan map observations and one for chopped/nodded observations) will operate on the corresponding detector and housekeeping timelines to produce detector data timelines calibrated in terms of in-beam source flux density.

Two options are considered for the photometer pipelines:

(ii) an "empirical" approach (Sections 5 and 6), similar to the data processing schemes traditionally used for bolometer instruments, in which the detector voltages are used directly to derive the astronomical signals, and which requires empirically-based corrections to be made in order to correct for thermal effects and non-linear response;

(i) a "model-based" approach which uses physical models of the bolometers and their operating temperatures, involves calculation of the absorbed radiant power as an intermediate step in the derivation of the astronomical signals, and is in principle capable of correcting for both thermal variations and detector non-linearity.

The model-based approach has potential advantages in that it automatically takes into account the detector bias conditions, non-linear response to strong sources, and any variations in detector bath temperature and background radiation from the instrument or the telescope. But implementing the model-based pipeline may be challenging, at least in the first instance, so it is planned that the empirical pipeline be implemented in full and available at the start of the mission. The empirical pipeline will therefore be implemented by the SPIRE ICC in preparation for launch and SPIRE operations. It may eventually be superseded eventually by the model-based pipeline.

2. List of symbols

Symbol	Definition
a	Detector slow response amplitude factor
A_{Tel}	Telescope effective collecting area
B	Calibration constant combining RSRF, telescope area and overall efficiency
C_H	Capacitance of the harness between the detector and JFET input
$\mathbf{C_{elec}}$	Electrical crosstalk matrix
$\mathbf{C_{opt}}$	Optical crosstalk matrix
DATA	16-bit ADC output value corresponding to a detector voltage value
e_{ij}	Coefficient of electrical crosstalk matrix linking output of detector i to detector j
f_b	Bias modulation frequency
f_{samp}	Detector sampling frequency
G_d	Bolometer dynamic thermal conductance (dW/dT)
$G_{d\text{-}300mK}$	G_d at 300 mK
G_{LIA}	Gain of signal chain between JFET output and low-pass filter output
G_{tot}	Total gain of analogue signa chain from JFET output to the ADC
$H_{Bol}(\omega_s)$	Bolometer transfer function with respect to modulated radiant power
$H_{BPF}(\omega_b)$	Transfer function of the DCU band-pass filter
$H_{Demod}(\phi)$	Square-wave demodulator transfer function as a function of input phase difference
$H_H(\omega_b)$	Transfer function of the harness between the detector and JFET input
$H_{JFET}(\omega_b)$	Transfer function of the JFET
$H_{LPF}(\omega_b)$	Transfer function of the DCU low-pass filter
H_o	Bandpass filter peak gain
$i_b(t)$	Bias current as a function of time
I_b	Bias current amplitude
$I_{b\text{-}RMS}$	RMS value of bias current
j	$\sqrt{-1}$
K_1, K_2, K_3	Parameters defining function fitted to variation of overall system responsivity (dS/dV) with operating point voltage
n_{samp}	Number of detector samples per BSM position in chopped mode
o_{ij}	Coefficient of optical crosstalk matrix linking output of detector i to detector j
OFFSET	4-bit offset used to generate offset voltage to be subtracted from LPF output voltage
P	Electrical power dissipated in the bolometer
$Q(t)$	Total radiant power absorbed by a bolometer as a function of time
Q_B	Background power absorbed by a bolometer
Q_C	Radiant power from the astronomical calibration source absorbed by a bolometer
Q_S	Radiant power from the astronomical source absorbed by a bolometer
R_d	Detector resistance
R_L	Total load resistance
R_S	Bolometer resistance parameter
$R(\nu)$	Relative Spectral Response Function of a photometer band
$S_S(\nu)$	Astronomical source in-beam flux density at frequency ν
$S_C(\nu)$	Astronomical calibration source in-beam flux density at frequency ν
S_{oR}, S_{oR}	Fictitious flux density offsets measured when chopping in the presence of an ambient background that is different in the two chop positions
S_b	Background sky in-beam flux density
S_A, S_B	Demodulated flux density measured for nod positions A and B
t	Time
t_{wait}	Delay between issue of BSM move command and first detector sample for the new position
T_b	Period of bias waveform (= $1/f_b$) [not to be confused with temperature]
T_g	Bolometer material band-gap temperature

T_o	Bolometer bath temperature
$T_{L\text{-}1}$	SPIRE FPU Level-1 temperature
T_{tel}	Telescope temperature
$v_b(t)$	Bias voltage as a function of time
V_b	Bias voltage amplitude
$v_d(t)$	Voltage across detector as a function of time
U	Bolometer small signal responsivity (V_S/Q_S)
V_{ADC}	Voltage input to the ADC, from which *DATA* is derived
V_{BPF}	Amplitude of voltage at the band-pass filter input
V_d	Amplitude of voltage across detector
$V_{d\text{-}RMS}$	RMS value of voltage across detector
V_{Demod}	DC voltage amplitude at demodulator output
V_{JFET}	Amplitude of the voltage at the JFET output
$V_{JFET\text{-}RMS}$	RMS voltage at the JFET output
V_{LPF}	Amplitude of voltage at the low-pass filter input
V_o	Fixed bolometer offset voltage used in flux density conversion.
V_{Offset}	Voltage level generated by the DAC from *OFFSET*, and subtracted from the LPF output voltage
V_S	Decrease in RMS detector voltage at the operating point due to the astronomical signal
$V_{th}(t)$	Array thermometry timeline used to remove corellated noise from the bolometer timelines
W	Total power dissipated in the bolometer
α_C	Astronomical calibration source power law spectral index
α_S	Astronomical source power law spectral index
α_{nom}	Nominal source spectral index for which SPIRE flux densities will be quoted
β	Bolometer thermal conductivity power law index
$\Delta V_{JFET\text{-}RMS}$(1-bit)	Change in RMS voltage at the JFET output that corresponds to a 1-bit change in the value of *DATA*
$\Delta\phi$	Phase difference between demodulator reference and input signals
ΔS	Statistical uncertianty in flux density
ϕ	Bolometer temperature normalised to the bath temperature
$\eta(\nu)$	Overall efficiency for coupling between flux density at the telescope aperture and power absorbed by a detector
τ_B , τ'_B	Bandpass filter time constant parameters
τ_1	Detector nominal time constant
τ_2	Detector “slow” time constant
ν	FIR/submm radiation frequency
ν_o	Radiation frequency characterising a photometer band, and for which the astronomical flux density is quoted
τ_H	Time constant defined by the JFET harness capacitance and the parallel combination of the detector and load resistances
σ	Signal-to-noise ratio
ω_b	Angular frequency of detector bias voltage
ω_S	Angular frequency of detector signal modulation

3. The SPIRE on-board electronics chain

The electrical design of the SPIRE detector subsystem and the on-board electronics is described in detail in the *SPIRE Design Description* document [4], and in the *DCU DD*. This section outlines the main features and functions of the system.

3.1 Bolometer bias and readout

Figure 1 shows the essential features of the bolometer bias and readout electronics used in SPIRE. The bolometer is biased (heated, by applied electrical power P, to its optimum operating temperature of around $1.3T_o$) by a sinusoidal excitation at angular frequency ω_b, corresponding to a frequency, $f_b = \omega_b/2\pi$, of around 100 Hz. The sinusoidal bias excitation is applied symmetrically via the two load resistors each with resistance $R_L/2$ (~ 10 MΩ each). The resistance of a SPIRE detector at the operating point, R_d, is typically 3 MΩ. The bias excitation is much faster than the thermal time constant, so that bias itself does not produce a temperature modulation, and the impedance of the detector at the bias frequency is also purely resistive. This AC biasing is preferred over DC bias as it up-converts the signal information to the bias frequency, getting well above the $1/f$ noise knee of the JFET readout amplifiers. With this arrangement, because of the inherently low $1/f$ noise of the bolometers, the $1/f$ noise knee of the system can be very low (less than 0.1 Hz).

The detector signals are fed to a pair of JFET source followers, and the JFET outputs are connected via the long cryoharness to the warm electronics.

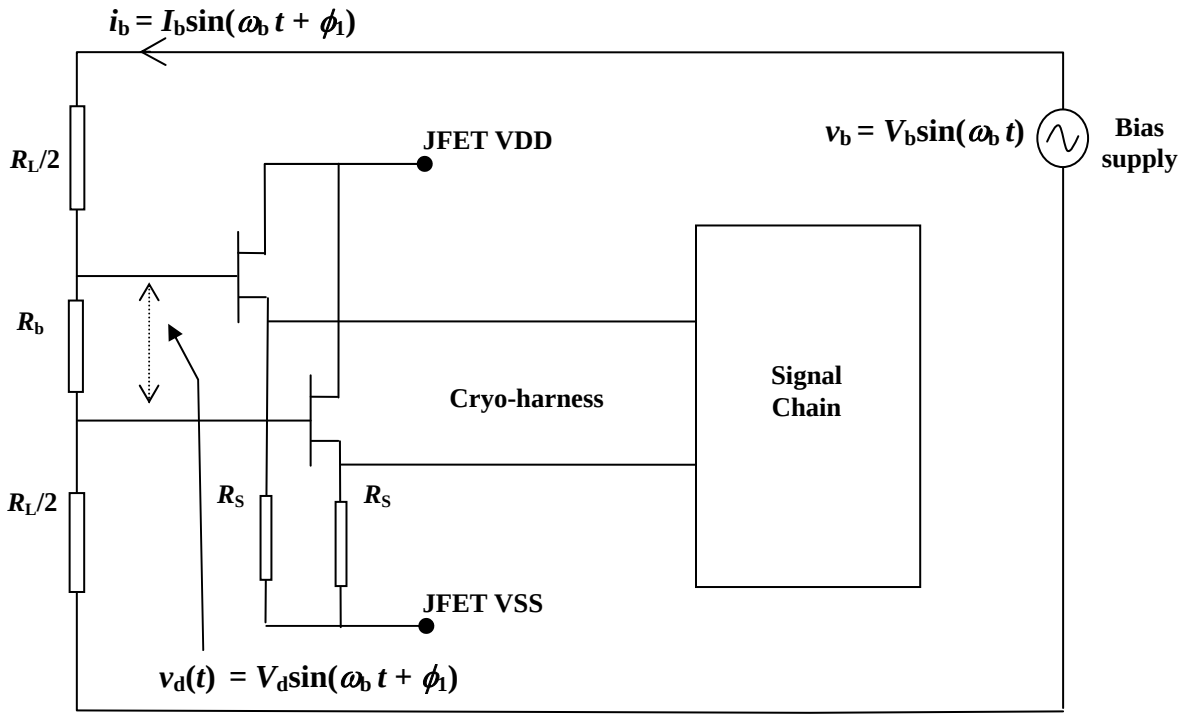

Figure 1: SPIRE bolometer bias and readout circuit

Let the applied AC bias voltage be

$$v_b(t) = V_b \sin(\omega_b t), \tag{1}$$

producing a bias current, flowing through the load resistor and the detector, given by

$$i_b(t) = I_b \sin(\omega_b t + \phi_1), \tag{2}$$

where ϕ_l is some phase difference between output of the bias generator in the warm electronics and the bolometer current.

The corresponding AC voltage across the detector is,

$$v_d(t) = V_d \sin(\omega_b t + \phi_l), \tag{3}$$

where $V_d = I_b R_d$.

The operating point on the load curve corresponds to the RMS values of the detector voltage and current:

$$V_{d\text{-RMS}} = \frac{V_d}{\sqrt{2}} \qquad I_{b\text{-RMS}} = \frac{I_d}{\sqrt{2}} \qquad P = V_{d\text{-RMS}} I_{b\text{-RMS}}. \tag{4}$$

The amplitude of bolometer signal, V_d, will vary if the radiant power on the detector is being modulated (for instance by chopping or telescope scanning in the case of the photometer or movement of the scan mirror in the case of the spectrometer. For a radiant signal modulated at frequency ω_S ($<< \omega_b$) we will represent the corresponding signal amplitude as $V_d(\omega_S)$.

3.2 Block diagram of the analogue electronics chain

A model of the complete SPIRE signal chain is shown in Figure 2. The detector signals are de-modulated by individual lock-in amplifiers (LIAs). An LIA comprises a bandpass filter and a square wave demodulator, followed by a low-pass filter. The output of the LIA is nominally a DC voltage proportional to the RMS value of the voltage at the bolometer output. The LIA outputs are multiplexed and sampled for telemetry to the ground. In order to achieve the necessary 20-bit sampling using a 16-bit ADC (the highest resolution available with space qualified devices), an offset subtraction scheme is implemented. The functions and characteristics of each element of the chain are described in the following sections.

3.3 Detector – JFET harness

The detector signals are fed to JFETs located outside the SPIRE Focal Plane Unit (FPU). The JFET input capacitance plus the stray capacitance of the harness between the detector and the JFET forms an *RC* filter with the parallel combination of the detector and the load resistance. This results in a some attenuation and phase change of the signal. Let the total capacitance (harness + JFET input capacitance) be C_H. The harness transfer function is represented as

$$H_H(\omega_b) = \frac{1}{1 + j\omega_b \tau_H}, \tag{5}$$

where $j = \sqrt{-1}$,

and $$\tau_H = \left[\frac{R_L R_d}{R_L + R_d}\right] C_H. \tag{6}$$

The magnitude of $H_H(\omega_b)$ is $$\left|H_H(\omega_b)\right| = \frac{1}{\left[1 + (\omega_b \tau_H)^2\right]^{1/2}}.$$

The values of C_H currently adopted are 50 pF for the photometer detectors and 20 pF for the spectrometer detectors. For R_L = 20 MΩ, R_d = 3 MΩ, and $\omega_b = 2\pi(130)$ rad s^{-1}, the corresponding value of $\left|H_H(\omega_b)\right|$, is 0.994 with a phase of about 6°.

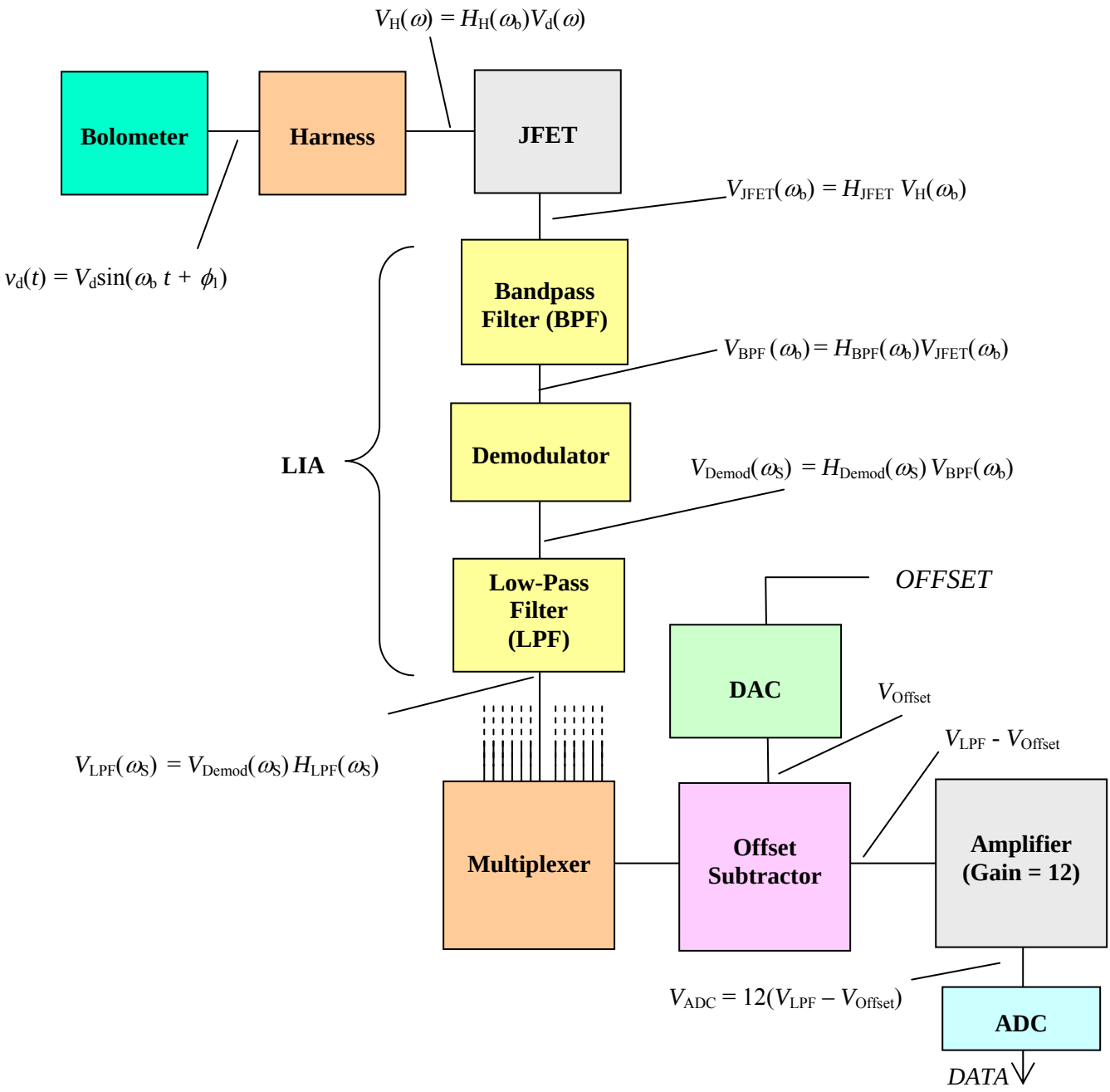

Figure 2: SPIRE bolometer signal chain.

3.4 JFETs

The output of the JFET source followers reproduce their input voltages, with a small attenuation, and – importantly – with a much lower output impedance than the detector. This allows the next stage of amplification to be located in the warm electronics (on the Herschel Service Module) with negligible attenuation due to capacitance of the several metres of cable in between.

The JFETs have a transfer function, H_{JFET}, which we take to be uniform over the range of bias frequencies used in SPIRE. The magnitude of H_{JFET} is slightly less than unity, and we also assume that it is the same for both JFETs in that pair. Currently, a representative value of $H_{JFET} = 0.96$ is adopted for all JFETs. It is planned to measure H_{JFET} explicitly for each channel, and a calibration table of gains will be produced.

The RMS voltage at the JFET output is

$$V_{\mathrm{JFET-RMS}}(\omega_b) = |H_H(\omega_b) H_{\mathrm{JFET}}| V_{\mathrm{d-RMS}} \,. \tag{7}$$

3.5 Lock-in Amplifier

The signal from the JFETs is demodulated by the LIA, which has three stages:

(i) a band-pass filter/amplifier to remove the DC component and amplify the signal;
(ii) a square-wave synchronous demodulator which rectifies the signal;
(iii) a low-pass filter which produces a low-frequency output proportional to V_d.

3.5.1 Band-pass filter

The transfer function of the SPIRE bandpass filter is given by

$$H_{\mathrm{BPF}}(\omega_b) = H_o \left[\frac{j\omega_b \tau_B}{1 + j\omega_b \tau_B + (j\omega_b)^2 \tau'_B \tau_B} \right] , \tag{8}$$

where H_o = 262.8 for the photometer detectors and 114.4 for the spectrometer detectors, τ_B = 4.7 ms, and $\tau'_B = 1.25 \times 10^{-4}$ s for the photometer and 6.68×10^{-5} s for the spectrometer (*DCU DD* p. 36; p. 54).

The magnitude of H_{BPF} as a function of bias frequency is plotted in Figure 3 for both the photometer and spectrometer. It is designed to be fairly flat across the range of bias frequencies that are expected to be used.

For the nominal photometer and spectrometer bias frequencies, we have:

Photometer (ω_b = 130 Hz): $|H_{\mathrm{BPF}}| = 259.61$;
Spectrometer (ω_b = 190 Hz): $|H_{\mathrm{BPF}}| = 113.81$.

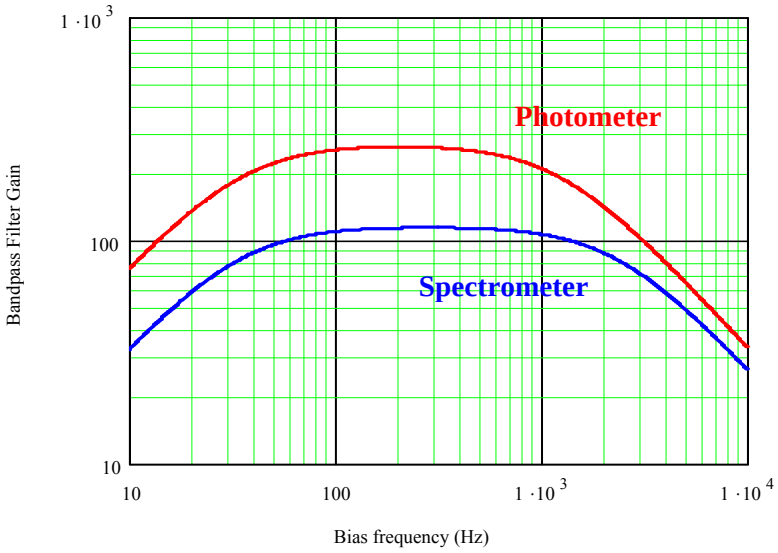

Figure 3: Magnitude of band-pass filter gain vs. bias frequency.

3.5.2 Square-wave demodulator

The demodulator multiplies the alternating input signal by a square wave reference voltage which is ideally in phase with the input signal, such that the multiplication factor is +1 during the positive half-cycle of the input and -1 during the negative half-cycle. It then functions as a perfect rectifier. Under these conditions, the DC or low-frequency component of the demodulator output is just the mean value of a rectified sine wave: $(2/\pi)V_{\mathrm{BPF}} = (0.637)V_{\mathrm{BPF}}$, where V_{BPF} is the amplitude of the input. But the output will be less than this

if the phase of the reference is not perfectly matched to that of the input. The (frequency-independent) transfer function, as a function of phase difference $\Delta\phi$, is given by

$$H_{\text{Demod}}(\Delta\phi) = \left[\frac{2}{\pi}\right]\cos(\Delta\phi)\,, \tag{9}$$

which is plotted in Figure 4.

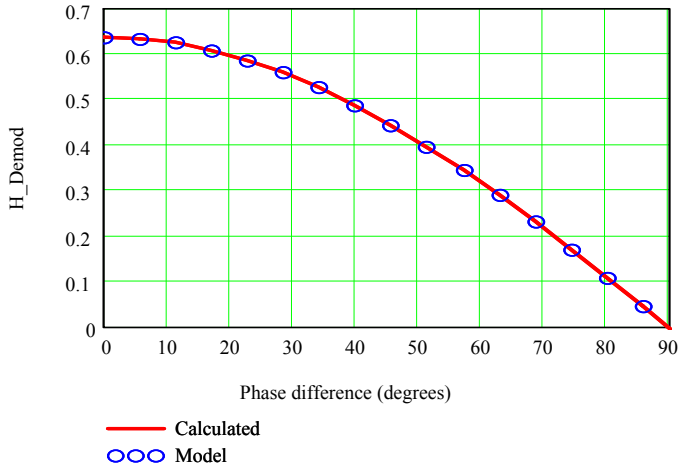

Figure 4: Demodulator gain vs. phase input difference. Red curve: gain as explicitly calculated by direct integration of the rectified waveform; blue dots: H_{Demod} as given by equation (9).

For the case of near zero ω_S (slowly varying radiant power), the demodulator output is a DC voltage related to the amplitude of the JFET output voltage by

$$V_{\text{Demod}}(\omega_b,\phi) = H_{\text{BPF}}(\omega_b)H_{\text{Demod}}(\Delta\phi)V_{\text{JFET}}\,, \tag{10}$$

so

$$V_{\text{Demod}}(\omega_b,\phi) = \sqrt{2}H_{\text{BPF}}(\omega_b)H_{\text{Demod}}(\Delta\phi)V_{\text{JFET-RMS}}\,. \tag{11}$$

If V_d is varying at angular frequency ω_S ($<< \omega_b$) due to detector radiant power modulation, then V_{Demod} will also vary accordingly.

The phase difference is dictated largely by the bolometer-JFET harness time constant, τ_H. In setting up the LIAs, the phase of the LIA reference can be adjusted for each array, so as to correct for the phase difference ϕ_1 in equation (2) and hence make $\Delta\phi$ equal to zero. In flight, it will be adjusted to make $\Delta\phi = 0$ for the nominal operating condition (telescope background; pointing at blank sky). There will be a slight degree of non-optimal phase due to the spread in detector impedances across the array. Furthermore, since the detector impedance varies with radiant loading, a component of phase mismatch will also arise when looking at bright sources. Let the nominal bolometer resistance be $R_{\text{d-nom}}$ (this will be the resistance when the telescope views dark sky). If the resistance changes significantly from this value (due for instance to a strong signal power), then a phase shift will be introduced:

$$\begin{aligned}\Delta\phi &= \tan^{-1}(\omega_b\tau_{\text{H-nom}}) - \tan^{-1}(\omega_b\tau_H) \\ &= \tan^{-1}\left(\omega_b\left[\frac{R_L R_{\text{d-nom}}}{R_L + R_{\text{d-mom}}}\right]C_H\right) - \tan^{-1}\left(\omega_b\left[\frac{R_L R_d}{R_L + R_d}\right]C_H\right).\end{aligned} \tag{12}$$

This phase difference will be small, and, as can be seen from Figure 4, its effect on the demodulator transfer function is also small. Nevertheless, it can be taken into account in the procedure for calculating the bolometer resistance (see Section 3.9).

3.5.3 Low-pass filter (LPF)

The low pass filter following the demodulator is designed to reject all higher-frequency components from the demodulator output, passing just the DC or slowly varying voltage directly proportional to the amplitude of the detector voltage. If the radiant signal on the detector is constant, then it will be just a DC component. If the radiation is modulated at angular frequency ω_S (within the filter passband) then there will be a corresponding LPF output at angular frequency ω_S.

For the photometer, the low-pass filters are implemented as 4-pole Bessel filters, with transfer function given by (*DCU DD* p.40):

$$H_{\text{LPF-P}}(\omega_S) = \left[\frac{1.93}{1 + j\omega_S\left(42.6\times10^{-3}\right) + \left(j\omega_S\right)^2\left(5\times10^{-4}\right)}\right]\left[\frac{1}{1 + j\omega_S\left(25\times10^{-3}\right) + \left(j\omega_S\right)^2\left(4\times10^{-4}\right)}\right] \times\left[\frac{1}{1 + j\omega_S\left(10^{-3}\right)}\right] . \quad (13)$$

and for the spectrometer, 6-pole Bessel filters are used, with transfer function given by (*DCU DD* p.53):

$$H_{\text{LPF-S}}(\omega_S) = \left[\frac{2.86}{1 + j\omega_S\left(7.85\times10^{-3}\right) + \left(j\omega_S\right)^2\left(1.6\times10^{-5}\right)}\right]\left[\frac{1}{1 + j\omega_S\left(3.25\times10^{-3}\right) + \left(j\omega_S\right)^2\left(1.09\times10^{-5}\right)}\right] \times\left[\frac{1}{1 + j\omega_S\left(6.26\times10^{-3}\right) + \left(j\omega_S\right)^2\left(1.47\times10^{-5}\right)}\right]\left[\frac{1}{1 + j\omega_S\left(10^{-4}\right)}\right] . \quad (14)$$

The magnitudes of these are plotted vs. detector modulation angular frequency (ω_S) in Figure 5 on linear and logarithmic scales.

For a bolometer channel with low ω_S (no or very slow modulation of the radiant power), the DC gain of the LPF applies:

$$\left|H_{\text{LPF-P}}(0)\right| = 1.93 \quad \text{for the photometer,}$$

and

$$\left|H_{\text{LPF-S}}(0)\right| = 2.86 \quad \text{for the spectrometer.}$$

The overall gain of the LIA chain, relating LPF DC output voltage to the RMS JFET output voltage is given by

$$G_{\text{LIA}}(\omega_b) = \frac{V_{\text{LPF}}}{V_{\text{JFET-RMS}}} = \sqrt{2}\, H_{\text{Demod}}(\Delta\phi)\left|H_{\text{BPF}}(\omega_b)\right|\left|H_{\text{LPF}}(0)\right| . \quad (15)$$

For perfect phasing of the demodulator, ($\Delta\phi = 0$) we have

$$G_{\text{LIA}}(\omega_b) = (0.9003)\left|H_{\text{BPF}}(\omega_b)\right|\left|H_{\text{LPF}}(0)\right| . \quad (16)$$

This overall gain is plotted against bias modulation frequency in Figure 6.

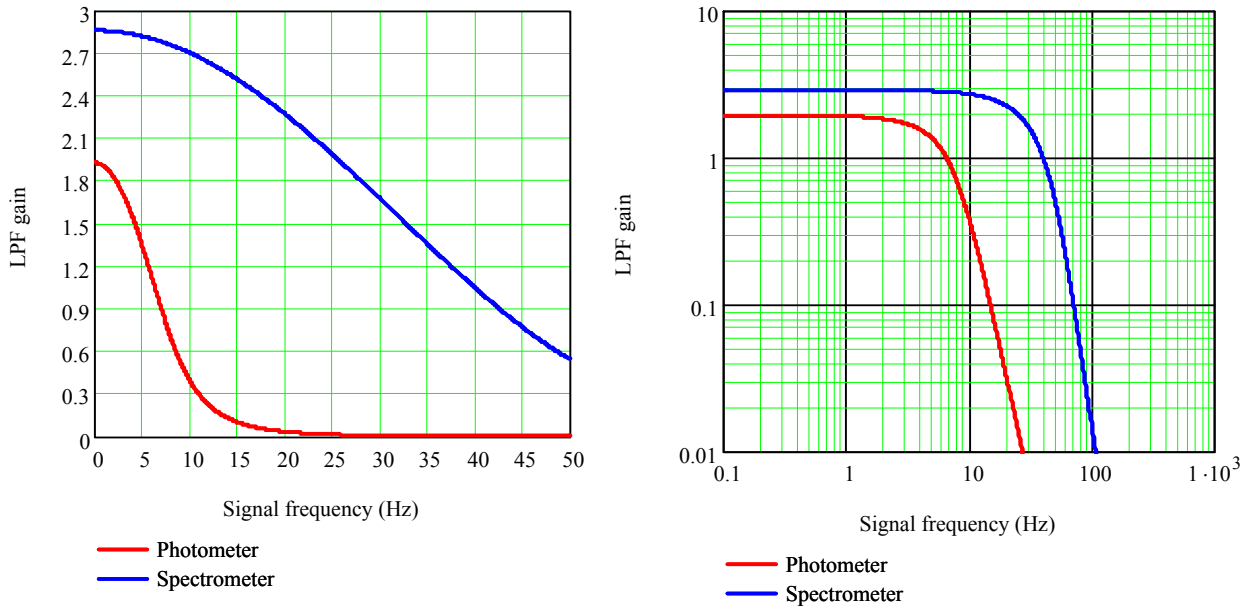

Figure 5: Low-pass filter gains as a function of detector signal frequency.

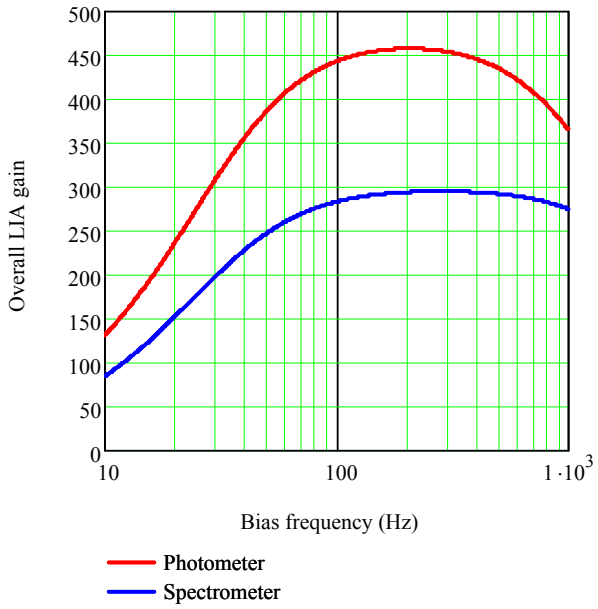

Figure 6: Overall gain of LIA signal chain, relating LPF DC output to the RMS voltage at the JFET output.

For example, taking our nominal bias frequencies of 130 Hz (photometer) and 190 Hz (spectrometer), we have:

Photometer:	G_{LIA} = (259.61)(1.93)(0.9003)	= 451.1	(see *DCU DD* p. 44);
Spectrometer:	G_{LIA} = (113.81)(2.86)(0.9003)	= 293.0	(see *DCU DD* p. 57).

3.6 Multiplexer

The LIA outputs are multiplexed in groups of 16 (photometer) or 12 (spectrometer). In the case of the photometer, a second stage of multiplexing combines three groups of 16 to form a group of 48 channels.

3.7 Offset subtraction

After multiplexing, a pre-determined offset is subtracted for each channel. Offset subtraction is needed because the signals need to be sampled with greater precision than the 16 bits available from the ADC. This is achieved by subtracting a suitable DC offset from each signal and adding in an additional gain stage before digitisation. The offset voltage is generated by the DCU from a 4-bit DAC with binary input value *OFFSET* (range = 0 – 15).

At the start of each observation, the value of *OFFSET* is set for each detector individually by the DRCU according to a procedure described in Section 3.8 below. It is not possible to change the offsets during an observation, so the settings must be able to cope with the entire range of detector power expected during the observation – this includes changes due to the astronomical signal (all observing modes) and due to signal offsets created by chopping (point source and jiggle-map modes).

After offset subtraction, the signal is amplified by a gain of 12 and then digitised, producing a binary output value *DATA*, with range 0 to $(2^{16} - 1)$, which is sent to the DPU for telemetry.

The total gain of the DCU chain is thus $G_{\rm tot}(\omega_{\rm b}) = 12 G_{\rm LIA}(\omega_{\rm b})$. For the nominal bias frequencies used above, we therefore have

Photometer:	$G_{\rm tot}$ = (12)(451.1)	=	5413	(see *DCU DD* p. 77);
Spectrometer:	$G_{\rm tot}$ = (12)(293.0)	=	3517	(see *DCU DD* p. 77).

For bias frequency $\omega_{\rm b}$, the RMS voltage at the BPF input (i.e., the JFET output) is related to the digital ADC output, *DATA*, and the offset level, *OFFSET*, by the following formula (*DCU DD* p. 77):

$$V_{\rm JFET-RMS}\left(\omega_{\rm b}, DATA, OFFSET\right) = \left[\frac{5}{G_{\rm tot}\left(\omega_{\rm b}\right)}\right]\left[\frac{DATA - 2^{14} + \left(52428.8\right)\left(OFFSET\right)}{\left(2^{16} - 1\right)}\right]. \qquad (17)$$

This voltage is in turn related to the RMS bolometer voltage by

$$V_{\rm JFET\text{-}RMS}\left(\omega_{\rm b}\right) = H_{\rm H}\left(\omega_{\rm b}\right) H_{\rm JFET}\, V_{\rm d\text{-}RMS}\,. \qquad (18)$$

To see how the RMS voltage at the JFET output is related to the ADC output and offset setting, $V_{\rm JFET\text{-}RMS}$ is plotted in Figure 7 for the case of the nominal photometer gain, $G_{\rm tot}$ = 5413 (note that the numbers given in the *DCU DD p. 77* correspond to the maximum gain of 5481). For $G_{\rm tot}$ = 5413, the full ADC range for each offset step is 0.92371 mV and the 15 available offset levels cover a range up to 11.824 mV, with some overlap between successive offset levels, as indicated in Table 1.

There are 2^{16} - 1 = 65535 ADC bits potentially available within each *OFFSET* range, so the voltage step corresponding to one bit is

$$\Delta V_{\rm JFET\text{-}RMS}(1\ {\rm bit}) = (0.92371\ {\rm mV})/(65535) = 14.09\ {\rm nV}\,. \qquad (19)$$

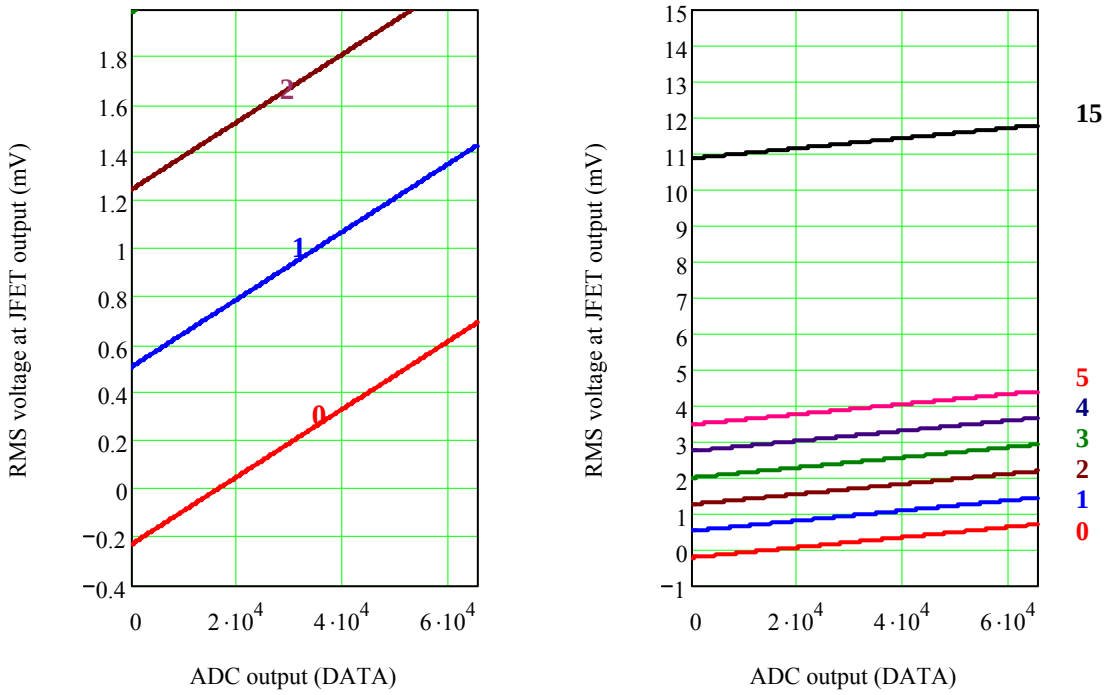

Figure 7: Photometer ADC output vs. JFET RMS output voltage for various values of *OFFSET* (for G_{tot} = 5413).

Offset =	Lower limit (mV) $V_{JFETrms}(0, Offset, G)$ =	Upper limit (mV) $V_{JFETrms}(2^{16}-1, Offset, G)$
0	-0.23093	0.69277
1	0.50804	1.43175
2	1.24702	2.17072
3	1.98599	2.90969
4	2.72496	3.64867
5	3.46394	4.38764
6	4.20291	5.12661
7	4.94188	5.86558
8	5.68086	6.60456
9	6.41983	7.34353
10	7.15880	8.08250
11	7.89777	8.82148
12	8.63675	9.56045
13	9.37572	10.29942
14	10.11469	11.03840
15	10.85367	11.77737

Table 1: $V_{JFET\text{-}RMS}$ range covered by each OFFSET value for the photometer with G_{tot} = 5413.

3.8 Offset setting procedure

Before each observation, the offsets are set for all detectors according to the procedure shown in Figure 8. Note that this procedure is the one actually implemented in the DRCU, and is different to the one described in the *DCU DD* (p. 126).

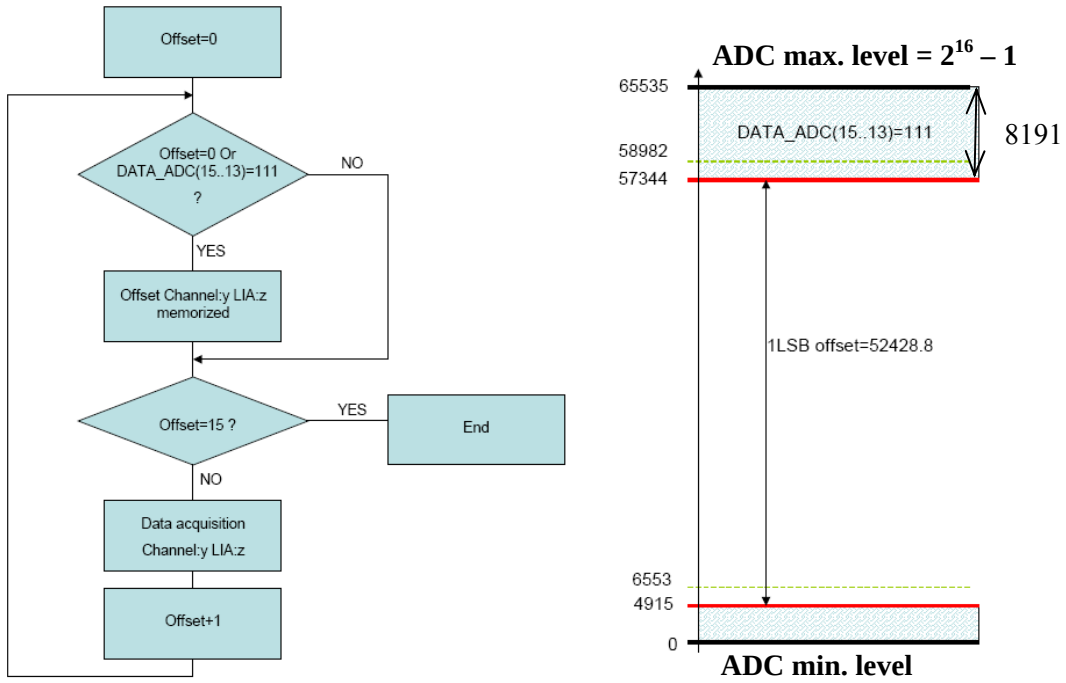

Figure 8: Procedure for setting the value of O*FFSET* and range of ADC output values corresponding to one offset setting.

For a given value of $V_{\text{JFET-RMS}}$ at the start of the observation:

1. *DATA* is a 16-bit number with range 0 to $2^{16} - 1$, with the bits numbered 0 – 15.
2. The 4-bit *OFFSET* is first set to 0000.
3. *OFFSET* is then incremented until the three most significant bits of *DATA* are not 111 (i.e. *DATA* < 57344) or *OFFSET* is 15.
4. At the end of this procedure, *DATA* has a value between 57344 and 4915.

This procedure is completely deterministic in that a given value of $V_{\text{JFET-RMS}}$ will result in a particular value of *OFFSET* being selected. Table 2 lists the selected *OFFSET* values as a function of $V_{\text{JFET-RMS}}$ for the case of the photometer with G_{tot} = 5413, and the chosen *OFFSET* is plotted against $V_{\text{JFET-RMS}}$ in Figure 9. The actual voltage range per level (i.e., upper – lower voltage for a given selected offset is 0.73898 V).

Note that when $V_{\text{JFET-RMS}}$ is just above an offset threshold, the value of *DATA* is 4195, and when it is just below an offset threshold, *DATA* is at its maximum allowed value (before changing the offset) of 57343.

If the voltage decreases during the observation (as will usually happen if the offsets are set off-source), then in the worst instance, the available dynamic range is 4915 bits. If the voltage decreases during the observation, the worst case dynamic range is 8191 bits.

To illustrate this, consider first the case of $V_{\text{JFET-RMS}}$ = 1.316296 mV (Table 2):

- This is just large enough to make *OFFSET* = 2, and the corresponding value of *DATA* = 4915
- For *OFFSET* = 2, the ADC zero level corresponds to $V_{\text{JFET-RMS}}$ = 1.2470170 mV (Table 1).
- The corresponding dynamic range is 1.316296 - 1.2470170 = 0.069279 mV.
- The same "worst case" dynamic range applies to all offset settings.

Now consider the case of $V_{\text{JFET-RMS}}$ = 1.316295 mV (Table 2)

- This is the highest value that will make *OFFSET* = 1, and the corresponding value of *DATA* = 57344.

- For *OFFSET* = 1, the ADC zero level corresponds to $V_{\text{JFET-RMS}}$ = 0.508044 mV (Table 1).
- The corresponding dynamic range is 1.316295 – 0.508044 = 0.808251 mV.
- The same "best case" dynamic range applies to all offset settings.

Offset o =	Voltage range (mV) for which this offset is chosen: vL_o =	vU_o =	ADC zero level for this offset: $V_{JFETrms}(0, Offset, G)$ =	ADC max. level for this offset: $V_{JFETrms}(2^{16}-1, Offset, G)$ =	G = 5413: $DATA(vL_j, j, G)$ =	$DATA(vU_j, j, G)$ =
0	-0.16165	0.577323	-0.230929	0.69277	4915	57344
1	0.57732	1.316296	0.508044	1.43175	4915	57344
2	1.31629	2.055269	1.247017	2.17072	4915	57344
3	2.05527	2.794242	1.985990	2.90969	4915	57344
4	2.79424	3.533215	2.724963	3.64867	4915	57344
5	3.53321	4.272188	3.463936	4.38764	4915	57344
6	4.27219	5.011161	4.202909	5.12661	4915	57344
7	5.01116	5.750134	4.941882	5.86558	4915	57344
8	5.75013	6.489107	5.680855	6.60456	4915	57344
9	6.48910	7.228080	6.419828	7.34353	4915	57344
10	7.22808	7.967053	7.158801	8.08250	4915	57344
11	7.96705	8.706026	7.897774	8.82148	4915	57344
12	8.70602	9.444999	8.636747	9.56045	4915	57344
13	9.44500	10.183972	9.375720	10.29942	4915	57344
14	10.18397	10.922945	10.114693	11.03840	4915	57344
15	10.92294	11.661918	10.853666	11.77737	4915	57344

Table 2: Offset values and the ranges of $V_{\text{JFET-RMS}}$ for which they are selected (photometer with G_{tot} = 5413).

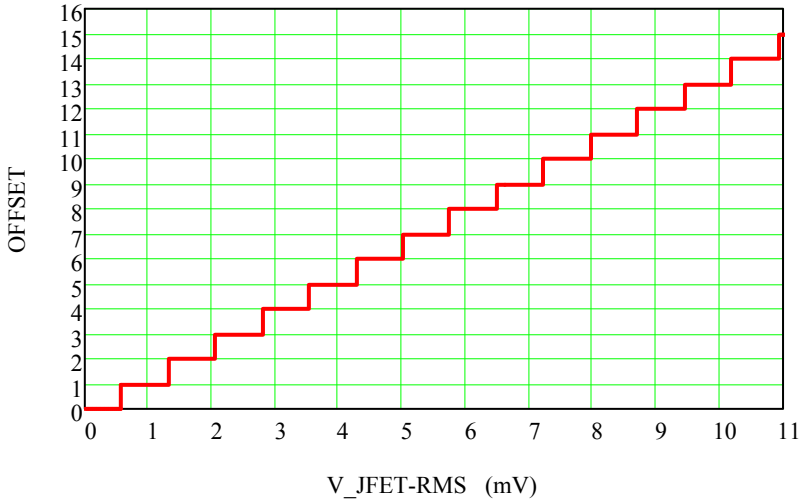

Figure 9: Selected *OFFSET* vs. $V_{\text{JFET-RMS}}$ (photometer with G_{tot} = 5413).

3.8.1 Offset setting for the photometer

Consider an observation during which the in-beam flux density will vary between $S_{\text{v-min}}$ and $S_{\text{v-max}}$. Before the observation, the *OFFSET* value will be set up for each detector, determined by its output voltage. Offsets can be set either off-source (default for the photometer) or on-source.

Off-source case: the nominal situation is that $S_v = S_{\text{v-min}} = 0$, so that $V_{\text{JFET-RMS}} = V_o$ at the telescope position for which the offsets are set. While the observations are in progress, the bolometer output voltage is always less than the value when the offset is selected - $V_{\text{JFET-RMS}}$ moves towards the zero level of the ADC, with a maximum change ΔV, as shown in Figure 10. The worst case dynamic range corresponds to the case in which the V_o is just above an offset threshold, so that *DATA* = 4915 and the difference between it and the value that will give *DATA* = 0 is at its smallest: the allowed drop in detector voltage during the observation is therefore at its smallest.

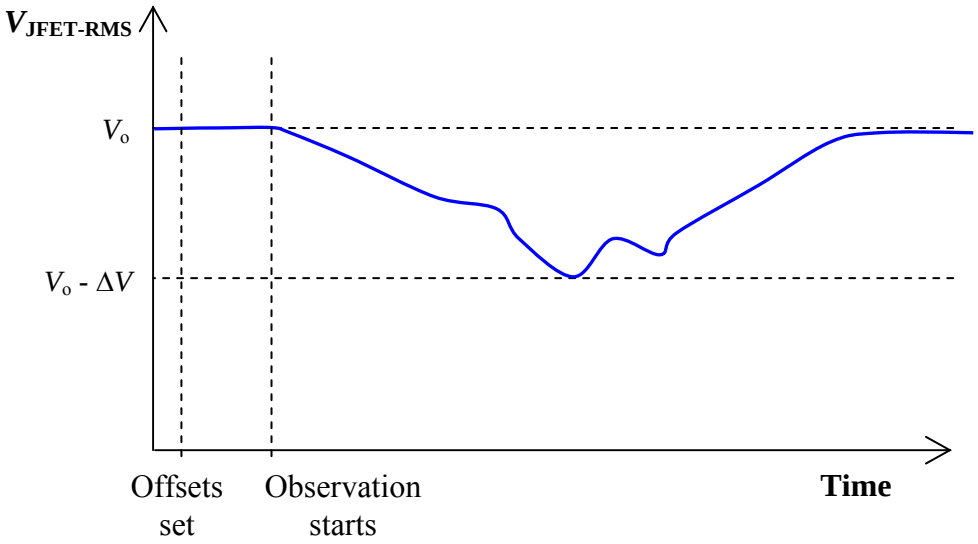

Figure 10: Example signal voltage timeline with offsets set at zero signal before the observation.

The worst case dynamic range is 4915 × $\Delta V_{JFET-RMS}$(1 bit) = (4915)(14.09 nV) = 0.06928 mV.

The best case dynamic range corresponds to the case in which the $V_{JFET-RMS}$ is just below an offset threshold, so that *DATA* = 57344 and the difference between it and the value that will give *DATA* = 0 is at its largest: the allowed drop in detector voltage during the observation is therefore at its largest.

The best case dynamic range is 57344 × $\Delta V_{JFET-RMS}$(1 bit) = (57344)(14.09 nV) = 0.80825 mV.

To get a rough estimate of the corresponding source brightness limits, the SPIRE photometer sensitivity model (assuming 20 mV RMS bias voltage for all arrays) has been used to derive the following information:

Band	Total background power (mainly from the telescope) (pW)	Astronomical gain (Jy pW^{-1})	Responsivity (MV W^{-1})	Worst case dyn. range of 0.06928 mV expressed in pW	Worst case dynamic range in Jy
PSW	1.2	137	320	0.217	(0.217)*137 = 30
PMW	1.0	250	330	0.211	(0.211)*250 = 53
PLW	1.7	226	350	0.199	(0.199)*226 = 45

So the worst case dynamic range corresponds to between about 30 and 50 Jy. The best case limits are about 12 times larger, so objects brighter than several hundred Jy will pose problems with saturation unless the detector bias is adjusted.

General case: Let the offsets be set at a position for which the flux density is some fraction *h* of the total range – i.e., $S_v = h(S_{v\text{-max}} - S_{v\text{-min}})$. The value of *h* can be different for each detector as they view different parts of the sky. $V_{JFET-RMS}$ can now increase of decrease during the observations, as shown in Figure 11.

In this case, the offsets are set at $V_{JFET-RMS} = V_o - h(\Delta V)$. The dynamic range requirement for increasing sky signal (decreasing output voltage) is now less than before, which is good. However, during parts of the observation, the voltage will also be higher than the initial value, by an amount up to $h(\Delta V)$. In the worst case, the available dynamic range for this is 8191 bits.

Since the dynamic range a the top of the ADC is better than at the bottom, it is better in principle to set the offsets on-source. However, since most photometer observations involve mapping and the position of peak brightness will not necessarily be known or easily identified, the default will be to set the offsets off-source (so that, $V_{JFET-RMS}$ only decreases during the observation).

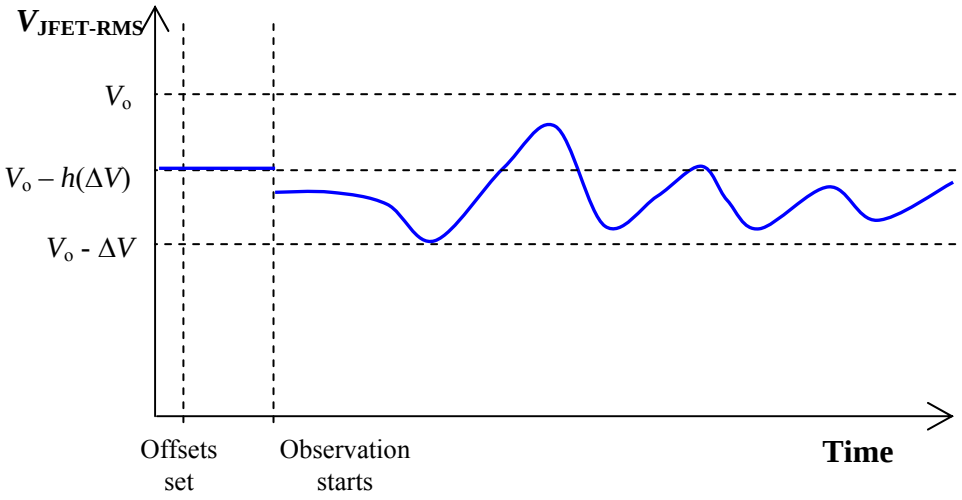

Figure 11: Example signal timeline with offsets set at an intermediate signal level before the observation.

3.8.2 Offset setting for the FTS

Assume for simplicity that the telescope is perfectly nulled by SCal (in practice there will be a small imbalance). Under that condition, an observation of blank sky results in a null interferogram – the power absorbed by the detector is constant throughout the interferogram at $(1/2)(Q_{Tel} + Q_{SCal}) = Q_{Tel}$, and the corresponding output voltage is constant at V_o. Now let a source be observed which results in an increase ΔQ in the broadband continuum power coming through the telescope. This will be split equally between the output ports, increasing the continuum power absorbed by the detectors. The unmodulated output voltage (corresponding to the DC level in the wings of the interferogram) will thus decrease by some corresponding – let this be $\Delta V/2$ (corresponding to $\Delta Q/2$).

When the mirror is scanned, the resulting interferogram represents the difference between the telescope and SCal input ports. One output port will correspond to (Telescope + Sky) – SCal, and the other to SCal – (Telescope + Sky). In the former case, the interferogram will have a negative-going central maximum (more radiant power), and in the latter case a positive-going central maximum (less radiant power). The peak height of the interferogram is equivalent to the continuum level, and so is also $\Delta V/2$. The two possible interferograms are illustrated in Figure 12. The total dynamic range that must be available to be able to cope with either case is V_o to $V_o - \Delta V$.

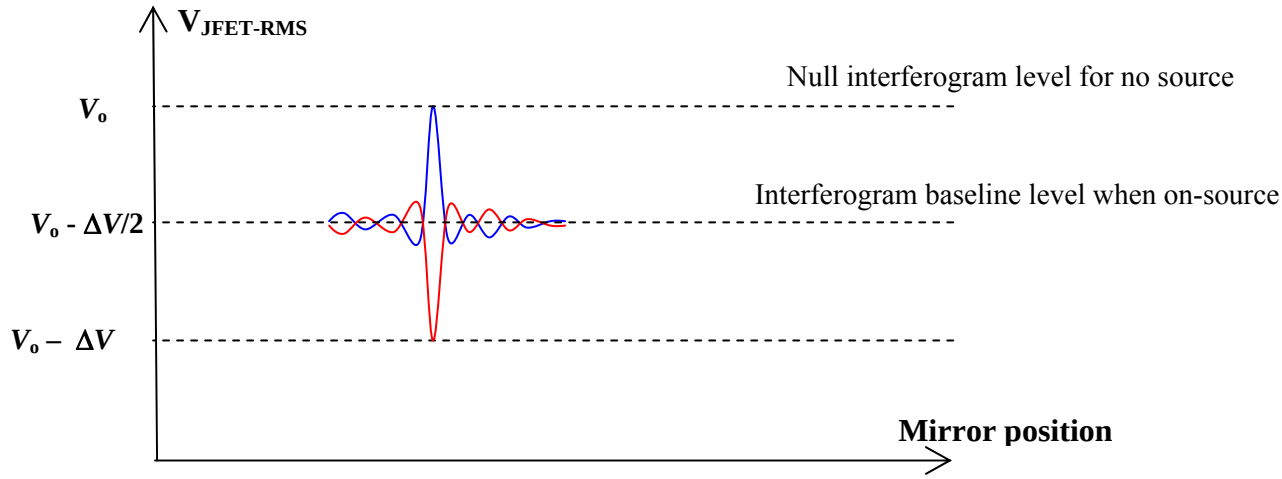

Figure 12: Interferogram dynamic range, assuming perfect telescope nulling. The output voltage is V_o for no source, and $(V_o - \Delta V/2)$ off ZPD when on source. The red interferogram is for the port corresponding to (Telescope + Sky) – SCal, and the blue is for the port corresponding to SCal – (Telescope + Sky).

Offsets set off-source (i.e., at V_o): The output voltage will always decrease. When the telescope is pointed on-source, the interferogram baseline level will be $V_o - \Delta V/2$, and we must be able to cope with a change of $\pm \Delta V/2$ about that level. In the worst case, with the offset set initially at the bottom of its range, the highest continuum level that can be coped with corresponds to (4915)/2 = 2458 bits.

Offsets set on-source (i.e., at $V_o - \Delta V/2$): The output voltage can now go up or down in the interferogram. If the offset is set at the bottom of the range, the output can go down by 4915 bits. If it is set at the top, the output can go up by 8192 bits.

So setting the offsets on-source has an advantage in terms of the worst-case dynamic range.

3.9 Measurement of detector voltage and resistance

From equation (17), the RMS voltage at the JFET output can be computed from the telemetry data value. This can be used to derive the detector voltage, current and resistance by an iterative procedure designed to take into account the *RC* roll-off due to the harness transfer function (equations 5 and 6) and also any changes in the phasing of the demodulator.

Step 1: Estimate $V_{\text{d-RMS}}$ and R_d, taking $H_H(\omega_b) = 1$:

$$V_{\text{b-RMS}} = \frac{V_{\text{JFET-RMS}}}{H_{JFET}}, \qquad I_{\text{b-RMS}} = \frac{V_{\text{b-RMS}} - V_{\text{d-RMS}}}{R_L}, \quad \text{and} \quad R_d = \frac{V_{\text{b-RMS}}}{I_{\text{b-RMS}}} - R_L . \tag{20}$$

Step 2: Estimate $H_H(\omega_b)$ and $\Delta\phi$:

$$\left|H_H(\omega_b)\right| = \frac{1}{\left[1 + (\omega_b \tau_H)^2\right]^{1/2}} \quad \text{with} \quad \tau_H = \left[\frac{R_L R_d}{R_L + R_d}\right] C_H , \tag{21}$$

and $\Delta\phi$ given by equation (12) in Section 3.5.2:

$$\Delta\phi = \tan^{-1}(\omega_b \tau_{\text{H-nom}}) - \tan^{-1}(\omega_b \tau_H) \quad \text{with} \quad \tau_{\text{H-nom}} = \left[\frac{R_L R_{\text{d-nom}}}{R_L + R_{\text{d-nom}}}\right] C_H .$$

In order to compute this correction, the value of $R_{\text{d-nom}}$ (the resistance when the telescope views dark sky) must be known.

Step 3: Recalculate $V_{\text{d-RMS}}$ and R_d:

$$V_{\text{d-rms}} = \frac{V_{\text{JFET-RMS}}}{H_{JFET}\left|H_H(\omega_b)\right|\cos(\Delta\phi)}, \quad I_{\text{b-rms}} = \frac{V_{\text{b-rms}} - V_{\text{d-rms}}}{R_L}, \text{ and } \quad R_d = \frac{V_{\text{b-RMS}}}{I_{\text{b-RMS}}} - R_L . \tag{22}$$

Continue iterating (repeat steps 2 and 3) until $I_{\text{b-RMS}}$ and R_d converge (criterion: change on iteration < 0.1%).

The RMS detector voltage is then just $$V_{\text{d-RMS}} = I_{\text{b-RMS}} R_d . \tag{23}$$

The timelines of voltage and current constitute the Level 0.5 Photometer Data Timeline (PDT) and Spectrometer Detector Timeline (SDT) products.

4. Photometer system transient response

The overall response of the system depends on the transient response characteristics of the detector and the low-pass filter. There is evidence from measurements on similar detectors (used on Planck-HFI, BLAST, and BICEP) that SPIRE-like bolometers may not exhibit a pure first-order response (characterised by a single time constant), but may also have a low-level slow response. Here we assume a variation of detector responsivity with frequency of the following form:

$$H_{\mathrm{Bol}}(\omega_s) = \frac{1-a}{1+j\omega_s\tau_1} + \frac{a}{1+j\omega_s\tau_2}. \qquad (24)$$

Typically, the primary time constant, τ_1, is about 6 ms for the photometer detectors and slightly lower for the FTS detectors. The "slow response" time constant, τ_2, can by several hundred ms, with the amplitude parameter a in the range 10 – 30%. The detailed slow-response characteristics of the SPIRE detectors have not been measured on the ground, so they will need to be measured during PV-phase through dedicated observations involving scanning point sources at various speeds.

4.1 Transient response in chopped photometry mode

The overall response to the astronomical power incident on the detector is determined by the transfer function given in equation (24) followed by that of the electronics chain. First, we assume no slow response component, and τ_1 = 6 ms. The overall response of the system in chopped photometry mode depends on the waveform of the astronomical signal and the transient response of the detector and the low-pass filter. The astronomical signal timeline is not a pure step function because of the BSM settling time. The BSM movement between the two chop positions is quite fast, typically about 10 ms to get within 2". For simplicity, we assume a point source observation with a chop throw of 163", and a linear relationship between position and time along the trajectory, corresponding to a BSM slew rate of 1.63 x 10^4 "/s. For a Gaussian beam of FWHM 24" (PMW), the corresponding timeline of astronomical power on the detector is as shown in Figure 13. The signal only begins to increase towards the end of the movement as the beam moves onto the source.

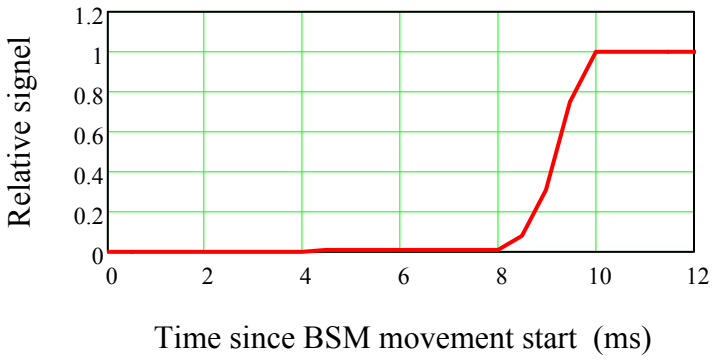

Figure 13: Simplified astronomical signal timeline for a PMW detector for a BSM movement starting at t=0.

The normalised response of the overall system to this input is shown in Figure 14. The low-pass filter dominates the shape of the transient, and causes the significant phase delay between the BSM movement and the signal waveform.

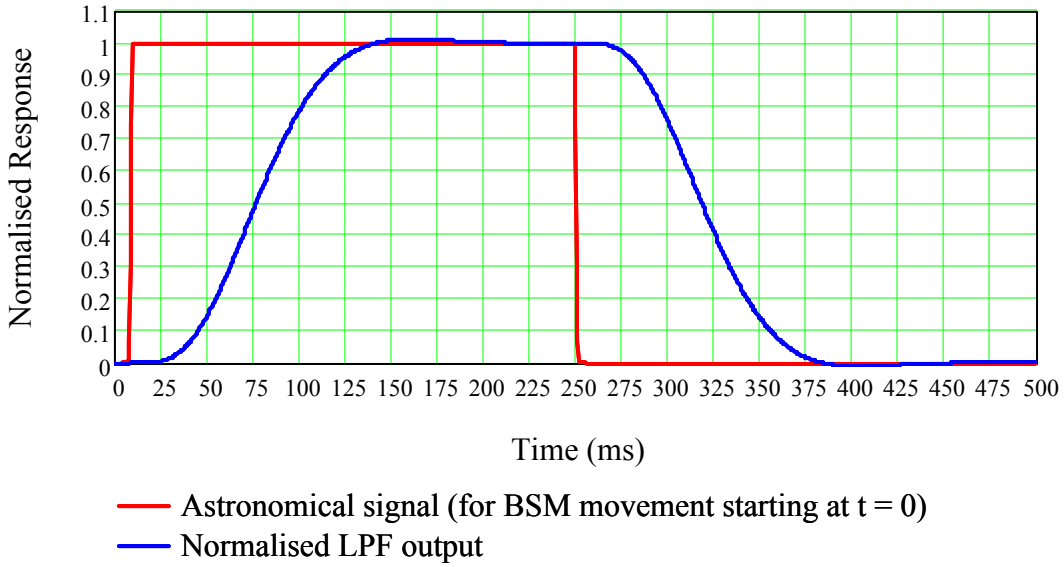

Figure 14: Overall transient response for BSM movements at t = 0 and t = 250 ms (corresponding to 2-Hz chop frequency). A pure first-order bolometer response is assumed (i.e., $a = 0$).

Figure 15 shows the overall response for the case of $a = 0.2$ and $\tau_2 = 0.5$ s. We see a reduced amplitude, since the slow component is mostly chopped out. However, it does impose a slope on the flat part of the waveform; and for the single chop cycle shown here, the system has not yet settled down.

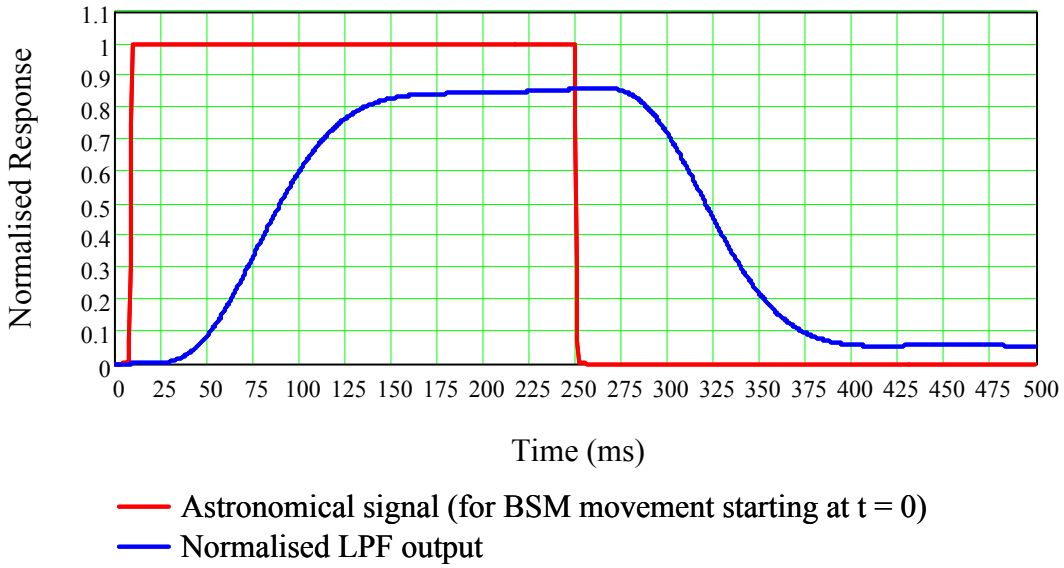

Figure 15: Overall transient response for BSM movements at $t = 0$ and $t = 250$ ms (i.e, 2-Hz chop frequency). A 20% slow bolometer response is assumed (i.e., $a = 0.2$), with a slow time constant of 0.5 sec.

4.2 Transient response in scan-map mode

Case of pure first-order detector response: First, we consider the case if a pure first-order bolometer response ($a = 0$). Spatial frequencies on the sky are encoded as electrical frequencies in the detector output in a manner that depends on the beam size and the telescope scan speed. For the fastest Herschel scan speed of 60" s^{-1} and the smallest SPIRE beam FWHM of 18" (for PSW), the beam crossing time is 18/60 s = 300 ms. The LPF has a 3-dB frequency of approximately 5 Hz, corresponding to a time constant of

approximately 30 ms. The basic detector time constant is typically 6 ms, so the filter would be the dominant effect, and with a time constant ~ ten times faster than the beam crossing time, the distortion is small.

Figure 16 shows the system response to a Gaussian astronomical signal, corresponding to a scan across a point source at 250 μm (18" FWHM) at 60" s^{-1}, with τ_1 = 6 ms. This is the worst case for SPIRE. The system response (black curve) is delayed by 74 ms and slightly attenuated (the delay will always be around this value, being dictated largely by the 5-Hz filter, with variations from one detector to another because of a spread of values of τ_1). For the nominal (30" s^{-1}) and fast (60" s^{-1}) scan rates, 74 ms corresponds to shifts in position of 2.2" and 4.4" respectively, which must be taken into account in the map-making process.

Figure 17 shows the residuals (delayed signal – system response) as a function of time during the scan. The signal loss at the peak is ~2%. The loss is even smaller for the longer wavelength channels and for slower scan speed, as summarised in Table 3.

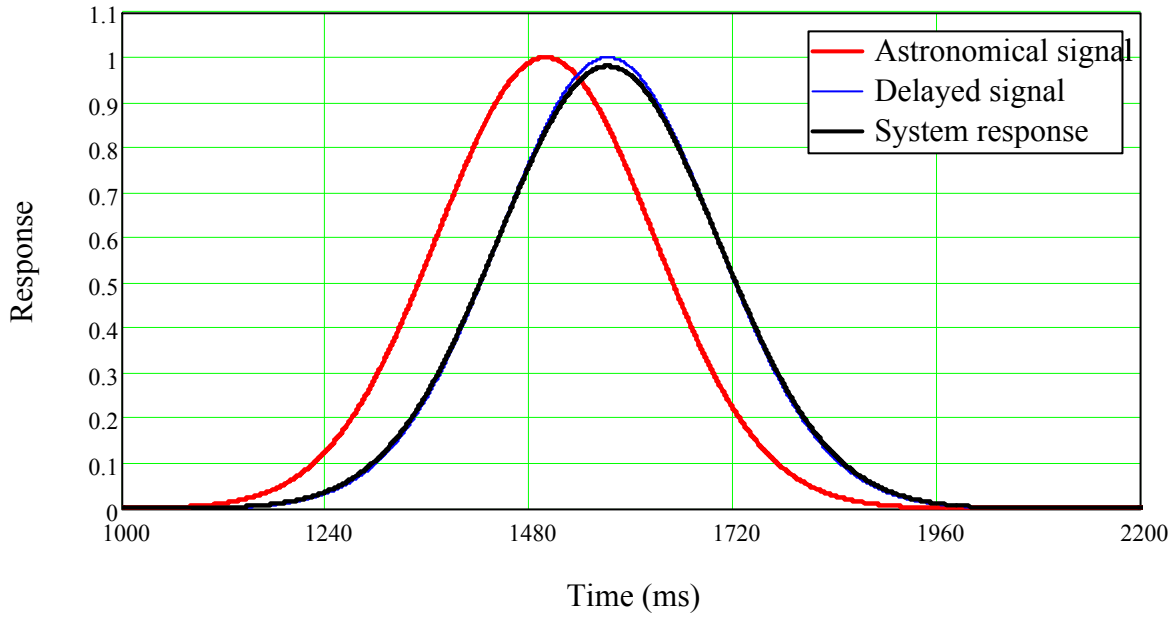

Figure 16: Signal chain response (black) to a Gaussian astronomical signal timeline (red) for a pure first-order detector response with τ_1 = 6 ms. The blue curve shows the signal timeline delayed by 74 ms.

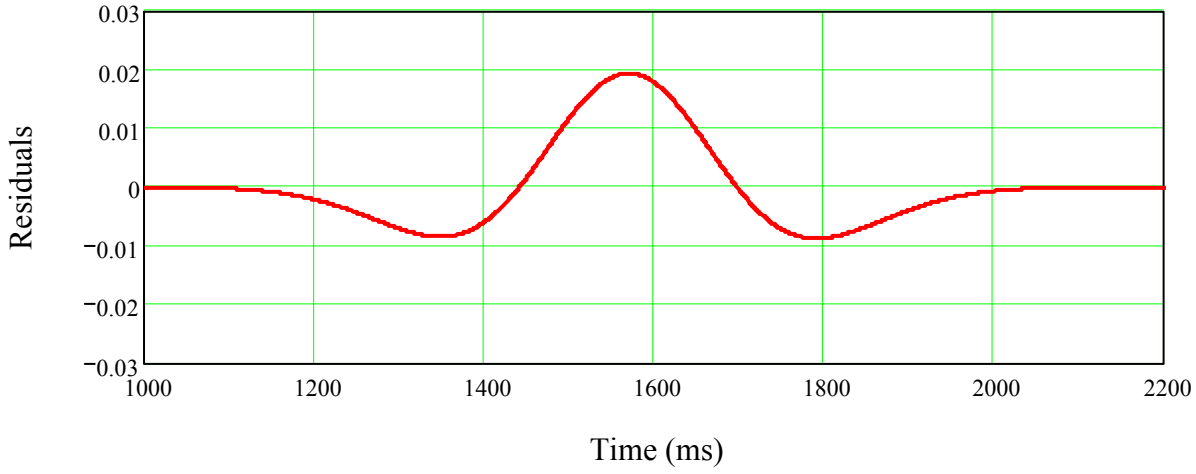

Figure 17: Difference between the delayed signal and the system response curves of Figure 16.

Scan speed (" s^{-1})	Beam FWHM (")	Peak loss (%)
30	18	0.5
	25	0.25
	36	0.12
60	18	1.9
	25	1.0
	36	0.5

Table 3: Percentage signal loss (with respect to a very slow scan) for scans across a point source in the three SPIRE bands, with scan rates of 30 and 60" s^{-1}.

Case of detector response with slow component: As an illustration of the impact of a slow component to the detector response, the example has been repeated but with a = 0.2 and τ_2 = 0.5 s. Figure 18 shows system response to a the Gaussian astronomical signal for 18" FWHM, 60" s^{-1} scan rate, τ_1 = 6 ms, τ_2 = 0.5 s, a = 0.2. The delay between the peaks is now about 80 ms and a loss of signal amplitude due to the reduction in the amplitude of the primary component. More significantly, there is also a long tail of response due to the slow component.

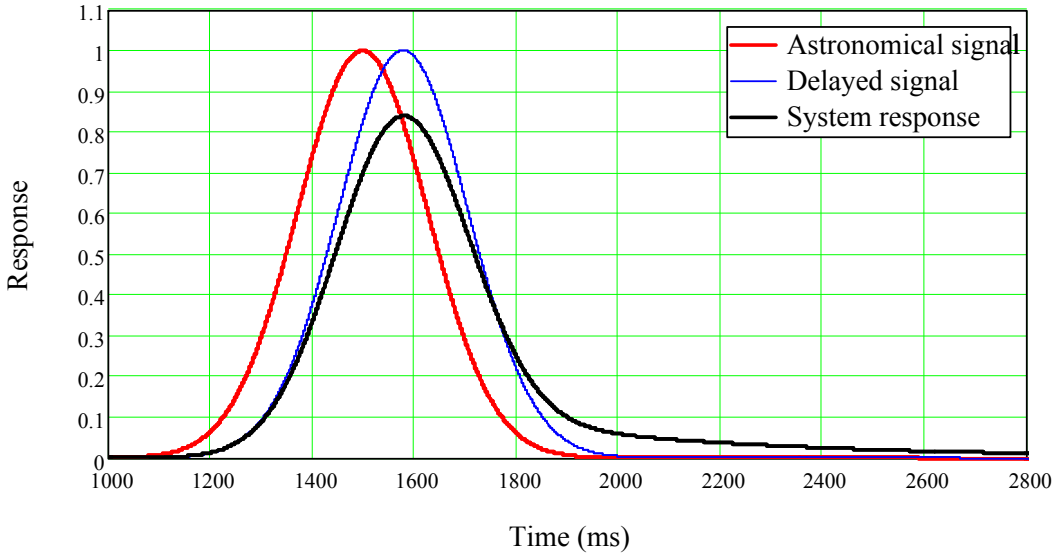

Figure 18: System response (black) to a Gaussian astronomical signal (red) for 18" FWHM, 60" s^{-1} scan rate, τ_1 = 6 ms, τ_2 = 0.5 s, a = 0.2. The blue curve is the astronomical signal delayed by 80 ms.

4.3 Detector sampling in chopped photometry mode

For detector sampling in chopped photometry mode, the sequence of events is as follows:

1. At a given time t = 0, the BSM is commanded to move (no BSM sampling or detector sampling is occurring).
2. The BSM move command is immediately followed by a command to start the BSM sampling (the delay to the first sample is always fixed).
3. After a fixed delay of t_{wait} to allow the BSM to settle down at its new position, a series of n_{samp} detector samples at frequency f_{samp} is commanded.

Note:

(i) The samples are automatically synchronised by the DCU electronics to the bias frequency f_b: the sampling frequency is always equal to the bias frequency divided by a whole number.

(ii) There are short delays (on the order of microseconds) associated with commanding and sampling - these are ignored here.

(iii) The nominal value of n_{samp} is 4 (i.e., 8 samples in total per BSM cycle) to ensure adequate sampling

of the waveform and to keep within the allowed data rate. With 2-Hz chop frequency and 4 samples per half-cycle, the samples are not statistically independent because of the integrating effect of the LPF – there is therefore little penalty in principle if they are not all used in the demodulation.

(iv) The actual time of the first sample will be greater than the time of the command due to the synchronism with the bias waveform. We assume that there will be a pseudo-random delay of up to one bias period, T_b, (typically 8 ms for a bias frequency of 130 Hz).

(v) The final sample in the set of n_{samp} need not be taken before the BSM is commanded to move again.

The chopped signal demodulation scheme (Section 6.6) must divide the signal waveform into two equal intervals phased in such a way as to maximise the demodulated signal level (i.e., it needs to be phase-synchronous).

Taking these considerations into account, the recommended sampling scheme for a particular case is described below. Note that this currently assumes no slow response – if there is a significant slow component, a problem may arise due to the sampling jitter because the "flat" part of the waveform is not flat. Implications of this for observing modes, data processing and photometric errors need to be assessed.

Bias frequency:	f_b = 130 Hz
Bias period:	$T_b = 1/f_b$ = 7.68 ms
Number of samples per BSM position:	n_{samp} = 4
Sampling frequency:	$f_{samp} = f_b/7$ = 18.60 Hz
Time between samples	$T_{samp} = 1/f_{samp}$ = 53.76 ms
Delay between BSM movement command and sample 1	t_{wait} = 95 ms
Commanded times of the eight samples	95.0 148.8 202.5 256.3 345.0 398.8 452.5 506.3 ms
Latest possible times of the samples	102.7 156.4 211.0 264.0 352.7 406.4 460.2 514.0 ms

The waveform and sample times are shown in Figure 19. The black and pink dots are separated by the bias period, T_b, and represent the extremes that may occur. Note that the possible delay in the range (0 – T_b) could be different for the positive and negative half cycles.

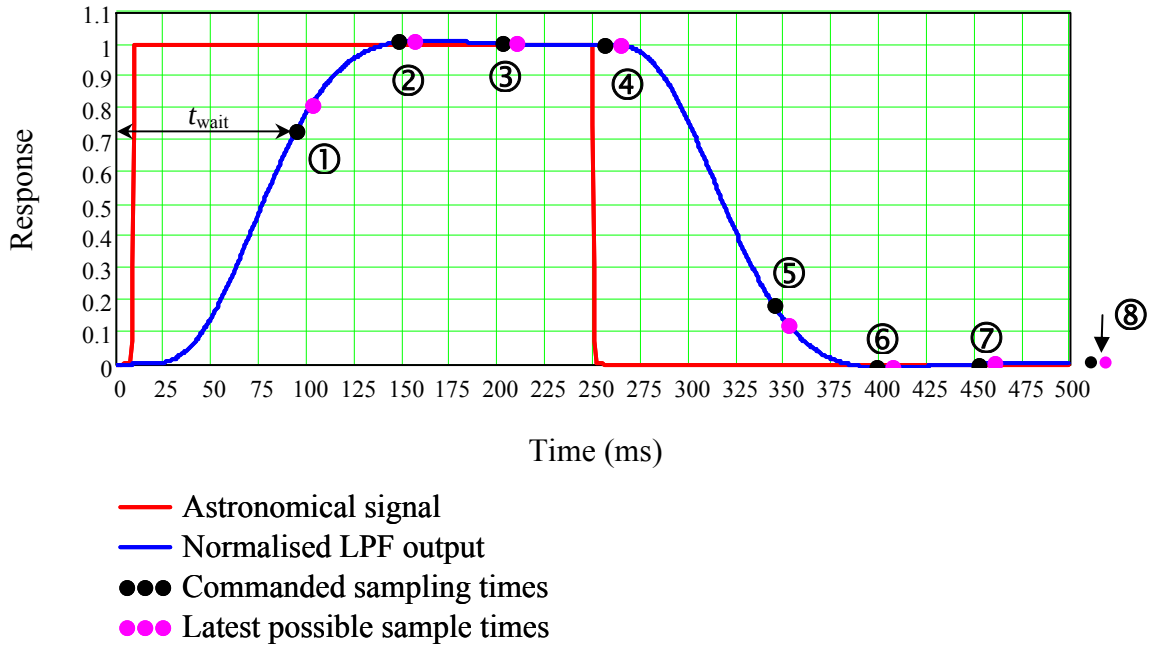

Figure 19: Eight signal samples over one BSM cycle for the example given in the text.

Because of the unpredictability of exactly when the samples are going to occur, the samples taken during the rise or fall period can vary significantly, making it inappropriate to use these for signal demodulation. Here we assume that the last three samples for each BSM position are to be used - i.e., samples sets (2, 3, 4) and (6, 7, 8) above.

In order to make the results insensitive to the potential variation in sampling times, it is necessary to optimise the delay between BSM motion and the initiation of the sampling sequence such that the three samples lie securely on the flat part of the waveform. Calculations have been done to determine the optimum value of t_{wait} and the corresponding variation in derived signal level arising from all possible combinations of delays in each half cycle. The demodulated signal varies by less than 0.1% over the whole range of possible sample distributions.

Note:

(i) although the first sample in each half cycle is not used explicitly in the demodulation, it can be used for monitoring/diagnostic purposes if appropriate;
(ii) the detailed sample timings will depend on the precise bias frequency and chop frequency adopted - the example above illustrates the method for devising the sampling and demodulation schemes;
(iii) it would be desirable to have five samples per half-cycle if the telemetry rate permits.

In the pipeline, the demodulation must be carried out in terms of flux density in order to preserve linearity under all circumstances.

4.4 Detector sampling in scan-map mode

During scan-map observations, the detectors will be sampled at 16 Hz. The time-shift between a sample and the corresponding position on the sky must be taken into account in the assignment of astrometric positions to the samples.

5. Scan-map pipeline

This section describes the various steps for the empirical scan-map pipeline. A number of these steps are the same in the jiggle-map pipeline described in Section 6.

Let the measured bolometer RMS voltage be

$$V_{\mathrm{d-RMS}} = V_{\mathrm{o}} + V_{\mathrm{S}}, \tag{25}$$

where V_{o} is the operating point voltage under identical operating conditions but in the absence of any astronomical signal, and V_{S} is due to the astronomical signal (V_{S} is actually negative as the bolometer resistance decreases with increasing absorbed power). The behaviour of the operating point voltage as the photometric background on the bolometer is changed is illustrated in Figure 20, which shows the form of the load curve under different conditions.

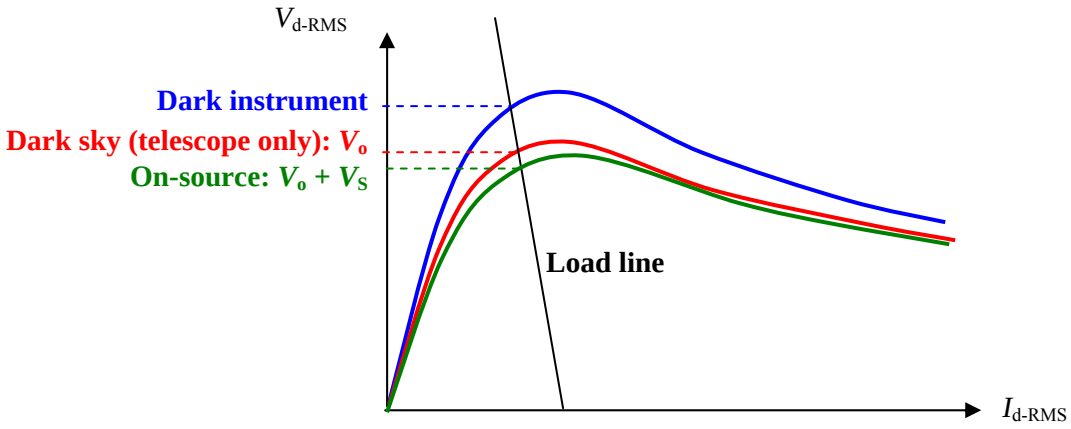

Figure 20: Dependence of operating point voltage on the operating conditions. V_{o} is the operating point voltage when viewing blank sky. V_{S} is the change from this voltage introduced by the source.

Note that:

(i) V_{o} depends on the bolometer parameters, operating temperature, and bias setting, and on the background power from the telescope;

(ii) V_{S} is linearly related to the source flux density for small signals, but there is a departure from linearity for large signals.

If V_{o} were known precisely, then it could be subtracted to allow a calculation of source flux density within the pipeline with no systematic offset. However, this is regarded as too ambitious, at least at this stage, because variations of V_{o} (with telescope background, instrument temperature and detector temperature) may be difficult to track. Therefore, a constant value will be assigned to V_{o} (for a given detector with a given bias setting). The V_{o} values for the detectors will be determined by a blank sky observation under the nominal operating conditions, and should thus be close to the ideal values. (The offset subtraction and the method of accounting for non-linear bolometer response are further discussed in Section 5.5.)

5.1 Scan map pipeline flow diagram

Figure 21 shows the sequence of steps in for scan-map pipeline, and the individual modules are described in the subsections below.

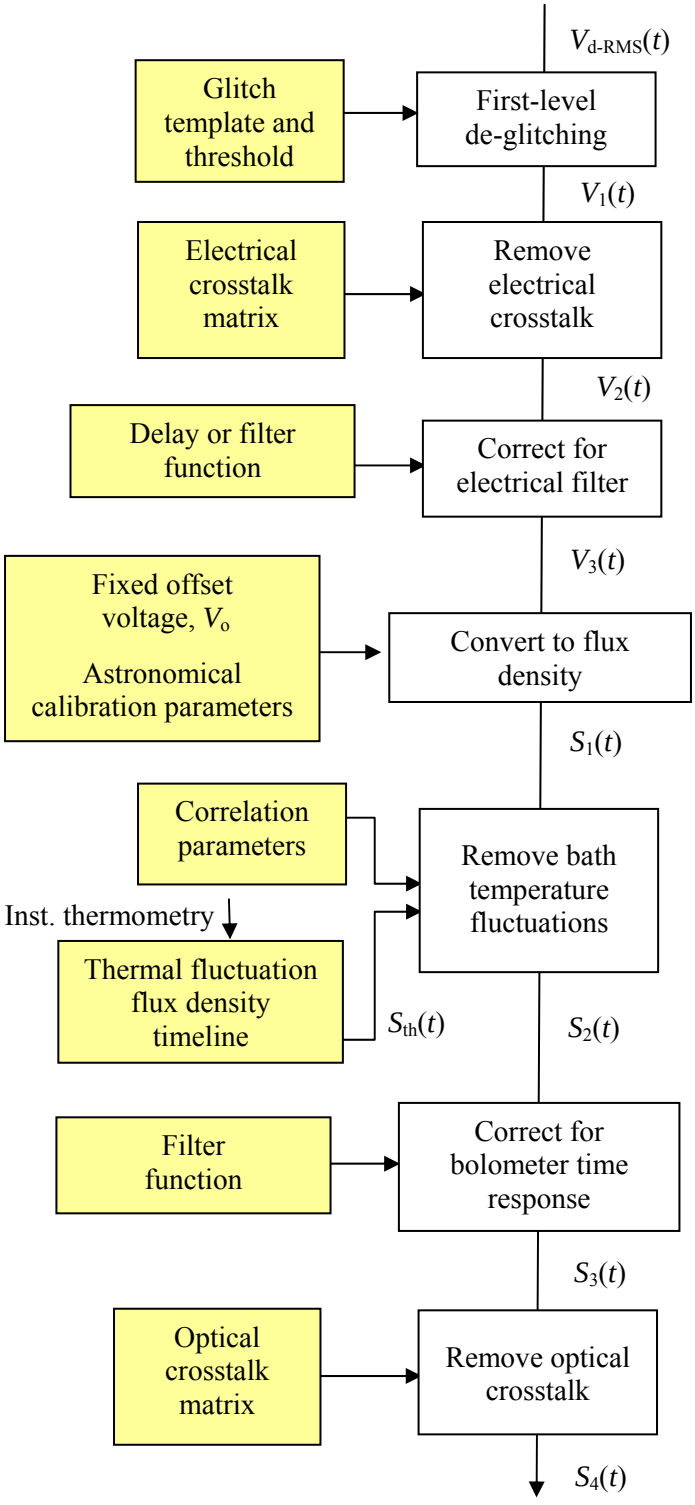

Figure 21: Empirical pipeline block diagram for scan-map observations.

The first three modules (first-level deglitching, removal of electrical crosstalk and correction for the electrical filter) are applied to the voltage timelines as they can be regarded as electrical effects. After subtraction of the operating point voltage, the timelines are converted to units of astronomical flux density, a process which includes subtraction of the fixed offset voltage, V_o, and correction for any non-linear response to strong astronomical signals. Corrections are then made for other effects (bath temperature fluctuations, bolometer response, and optical crosstalk) which are linear when applied in terms of the power absorbed by the bolometer (which is proportional to flux density).

5.2 First-level deglitching

Before further processing of the measured detector voltage timeline, $V_{\text{d-RMS}}(t)$, glitches due to cosmic ray hits or other impulse-like events in the detectors will be removed. Two options are considered:

Option 1: A simple algorithm is implemented in which the signature of the system response to an impulse (above some specified threshold which will depend on the noise level) is registered. The corresponding data samples are removed from the timeline and/or flagged as corresponding to a glitch. The deglitching scheme should involve:

- flagging as bad any samples that are at the ADC floor or ceiling levels;
- flagging as bad any of the three samples per half-cycle which deviates from the others by more than a pre-set threshold.

Option 2: A more sophisticated approach is described in Ref. [2] and proposed for the FTS, based on a local regularity analysis combined with a wavelet analysis. This scheme needs to be evaluated for use in the photometer pipeline. In principle, the same method should be applicable in both pipelines.

For the moment, we assume that Option 2 is also to be implemented for the photometer scan map mode.

The output of this module is the de-glitched voltage timeline, $V_{\text{1-i}}(t)$ for detector i.

5.3 Removal of electrical crosstalk

After de-glitching, let the timeline for bolometer i be denoted $V_{\text{1-i}}(t)$. It might contain contributions that depend on the signals from other detectors due to either electrical or optical crosstalk. Electrical crosstalk arises after the detector and is due to capacitative or inductive coupling between the detector readout channels. Optical crosstalk occurs before the detector and is due to diffraction or aberrations in the optical system causing some of the power from an astronomical source to fall on inappropriate detectors.

Electrical crosstalk can be removed if the coupling between the detectors is known, and it is appropriate to do it at this stage. The removal of optical crosstalk can only be done after the constant telescope background has been subtracted (see Section 5.8).

Here we assume that

(i) electrical crosstalk is linear, so that the effects can be characterised by a crossstalk matrix, $\mathbf{C}_{\text{elec}}$, with constant elements;
(ii) electrical crosstalk from one detector to another involves negligible diminution of the signal in the primary detector;
(iii) there is no crosstalk between different arrays.

For a particular time-step, the vector of electrical crosstalk-corrected signals is given by

$$\mathbf{V_2} = \mathbf{C_{elec}}\,\mathbf{V_1}\,. \tag{26}$$

As an illustration, if we had three detectors, the matrix equation would be

$$\begin{bmatrix} V_{2-1} \\ V_{2\text{-}2} \\ V_{2-3} \end{bmatrix} = \begin{bmatrix} 1 & e_{21} & e_{31} \\ e_{12} & 1 & e_{32} \\ e_{13} & e_{23} & 1 \end{bmatrix} \begin{bmatrix} V_{1-1} \\ V_{1-2} \\ V_{1\text{-}3} \end{bmatrix}. \tag{27}$$

The electrical crosstalk matrix can be implemented as a calibration file. Determination of the elements of the electrical crosstalk matrix is a difficult problem. One possibility is to use the occasional ionising radiation

hits that the bolometers will experience. Ideally, a single event in a bolometer produces a spike only in its own output; crosstalk results in this being accompanied by lower-level responses from other detectors.

In the absence of crosstalk, or if the crosstalk correction is to be left out, then the e_{ij} coefficients are set to zero.

The crosstalk corrected timeline for detector i is denoted $V_{2\text{-}i}(t)$.

5.4 Correction for electrical filter response

As shown in Section 4.2, the electronics chain imposes a delay on the data with respect to the telescope position along the scan; this effect must be taken into account to ensure that the astrometric pointing timeline is properly matched to the detector data timeline. Correction for the bolometer response is done later in the pipeline. To correct for the effect of electrical filter alone, there are two options:

Option 1:
(i) Fourier transforming each detector timeline $V_{2\text{-}i}(t)$;
(ii) multiplying the FT by an appropriate correction function $CF_i(\omega)$, based on the LPF transfer function;
(iii) transforming back to the time domain to obtain the corrected signal voltage, $V_{3\text{-}i}(t)$.

The relevant calibration information is the correction function, which will be derived from calibration file parameters stored for each detector (LPF transfer function parameters) - nominally the same for all detectors.

Option 2:
An alternative approach, which is simpler and almost as accurate is to impose a fixed delay to the timeline based on the response of the system to a Gaussian input. As shown in Section 4.2, implementing a delay of 74 ms results in less than 0.5% distortion for the nominal scan speed of 30" s^{-1}, and less than 2% for 60" s^{-1}. There are two options for the format of the output timelines:

(i) keep the detector samples and change the timestamps by subtracting the fixed delay from each;
(ii) keep the timestamps and interpolate to derive corrected detector samples.

The nominal sampling rate is 16 Hz. The sampling interval is thus 62.5 ms, so the delay is not an integer number of samples. The worst-case (PSW) number of samples per FWHM-crossing time is 9.6 for 30"/s and 4.8 for 60"/s. So in all cases, the sampling of the response to a point source is better than Nyqvist. It is therefore acceptable to implement the delay by interpolation between samples if desired (TBC by analysis/simulations)

As the baseline, Option 1 will be implemented (TBC when it has been confirmed that there are no technical impediments and that the noise level is not degraded). The output timelines should contain the original timestamps with modified detector signal values attached.

The filter corrected timeline for detector i is denoted $V_{3\text{-}i}(t)$.

5.5 Conversion to flux density

This section describes the method to be used to derive the in-beam flux density, including flat fielding and strong source corrections.

For an NTD bolometer with a given applied bias voltage, the small-signal responsivity varies with the voltage across the bolometer with an approximately linear relationship over a wide range background loading and bath temperature conditions [5]. This translates to a corresponding relationship for the differential sensitivity of the system to flux density, S. Writing $V_{d\text{-}RMS}$ as V, we have

$$\frac{dV}{dQ} \propto V \quad \Rightarrow \quad \frac{dV}{dS} \propto V \ . \tag{28}$$

To allow for the fact that the responsivity–operating point voltage relationship will not be exactly linear, we let

$$\frac{\mathrm{d}S}{\mathrm{d}V} = f(V), \tag{29}$$

The function $f(V)$ is specific to a particular detector and bias setting. In order to perform integration of $f(V)$, we can fit an approximating function to it. In comparison to polynomial fits with the same number of free parameters, we find more accurate fits to the predicted shape of $f(V)$ using a function of the form:

$$f(V) = K_1 + \frac{K_2}{V - K_3}, \tag{30}$$

where K_1, K_2 and K_3 are constants. K_1 has units of Jy V^{-1}, K_2 has units of Jy, and K_3 has units of V. If the responsivity were constant, then we would have $f(V) = K_1$.

K_3 and the ratio K_1/K_2 can be found by pointing the telescope at a selection of bright sources (without chopping) and measuring the relative change in responsivity as a function of bolometer voltage using PCal. It is not necessary to know how bright all the sources are – they are just being used to establish a range of backgrounds on the detectors. The effect of bright source on responsivity can also be simulated by raising the bolometer bath temperature. The absolute values of K_1 and K_2 can be determined by observation of a suitable astronomical calibrator. The characterisation of the responsivity as a function of operating point voltage using PCal is not model-dependent or sensitive to the bolometer or instrument temperatures obtaining during the calibration measurements. The signal from a faint source observed with a certain operating point voltage can also be converted to any other operating point voltage.

The derivation of the K-values and the astronomical calibration scheme are described in more detail in Section 7.1

A flux density corresponding to a measured RMS detector voltage, V_m, can be derived by integrating the above expression between some fixed detector voltage, V_o, and V_m:

$$S = \int_{V_\mathrm{o}}^{V_\mathrm{m}} f(V)\mathrm{d}V \ . \tag{31}$$

Ideally, V_o should be the bolometer voltage in the absence of any astronomical signal (i.e., what would be measured when observing blank sky in otherwise identical conditions). The resulting flux density would correspond to that from the sky calibrated with respect to the dark sky level. V_o will therefore be derived from standard calibration observations of a "dark" area of sky in scan-map mode, to produce a calibration file containing the offset voltages, $V_{\mathrm{o}\text{-}i}$, for the detectors under the nominal conditions: bias voltage and frequency; detector and instrument FPU (Level-1) temperature, and telescope temperature. Although ideally the conditions would be the same for the calibration and science observations, small differences are likely in practice. We therefore expect V_o will differ from the ideal value (by an amount much larger than most astronomical signals). This means that the initial flux density values produced in this step will have offsets that must be removed later to derive the flux density from the sky. The most effective approach is to do this as part of the map-making process. With cross-linked maps, which are recommended for most scan-map observations, this is done naturally as part of the map-making routine.

Following this treatment, the detector voltage is converted to a first estimate of flux density, S_1, by integrating $f(V)$ between the limits V_o and V_3:

$$S_1 = \int_{V_o}^{V_3} \left(K_1 + \frac{K_2}{V - K_3} \right) dV \qquad (32)$$

So
$$S_1 = K_1 (V_3 - V_o) + K_2 \, ln\left(\frac{V_3 - K_3}{V_o - K_3} \right) . \qquad (33)$$

Note that

(i) in the limit of very small signals, and if V_o, represented the bolometer voltage under identical conditions except viewing blank sky, then K_1 would correspond to the overall astronomical gain factor of the system (Jy V^{-1}) in the linear regime, as often quoted for ground-based instruments;

(ii) $f(V)$ is negative (nominally $V_3 < V_o$ since absorbed power causes a decrease in bolometer voltage).

The output of this module is a set of timelines corresponding to the first estimates of flux densities: $S_{1\text{-}i}(t)$ for detector i.

5.6 Removal of correlated noise due to bath temperature fluctuations

To first order, bath temperature fluctuations will influence all detectors in an array coherently – the temperature and corresponding output voltages will go up and down in synchronism. The bath temperature, T_o, may fluctuate due to temperature drifts within the instrument.

For the level of fluctuations expected in SPIRE, the most important effect of bath temperature variations will be the direct response of the detector output voltage. There will be a small second-order effect on the detector small-signal responsivity. Fluctuations in T_o are expected to be much slower than the nominal chopping frequency of 2 Hz, so that the correction will only be needed for scan-map observations. There are two options for removing the correlated thermal noise contributions to the bolometer timelines:

1. use of the correlations between the detector outputs themselves;
2. use of the correlations between the detectors and the array thermometers or blind pixels.

For Option 1, the procedure is as follows:
- take the median signal timeline of all the detectors in an array (or perhaps a set of them around the periphery of a "source" – but that has to be done at the level of the map rather than the timeline);
- adjust the median timeline so that its mean is zero;
- subtract this from each individual detector timeline

This method will not introduce much additional noise as the timeline to be subtracted is averaged over many detectors. However, there are two problems with this method: firstly, for scanning observations, large-scale sky structure can mimic bath temperature fluctuations (all the detectors going up and down together) and so can be removed by this process; secondly, the presence of strong emission in a part of the map will bias the median timeline, resulting in potential removal of some real signal.

Option 2 involves generating a voltage timeline $V_{th\text{-}i}(t)$ from the array thermometer timelines. A scaled version of this is then subtracted from that detector's signal timeline. To avoid introducing additional noise, the thermometry timeline will need to be significantly less noisy than the bolometer signals. It will therefore need to be averaged over a period of time such that it becomes a negligible fraction (say 10%) of the detector noise. This will require a suitable averaging period (JPL/IPAC assessment of the ILT data indicates that a period on the order of a second or a few seconds is suitable). Thermal fluctuations on timescales shorter than this will not be tracked.

In order to have a scheme that does not involve potential loss or distortion of the astronomical signal, Option 2 is to be adopted as the baseline. The detailed implementation will be defined by JPL/IPAC following evaluation and refinement of the method using ILT data.

The output of this module is a set of timelines of astronomical flux densities corrected for low-frequency thermal drifts: $S_{2\text{-}i}(t)$ for detector i.

5.7 Correction for bolometer time response

The bolometer transfer function is represented as a two-component system as described in Section 4. The baseline plan to correct for the slow detector time constant is to use the following procedure:

(iv) Fourier transforming each signal timeline $S_{S2\text{-}i}(t)$;
(v) multiplying the FT by an appropriate correction function $CF2_i(\omega)$;
(vi) transforming back to the time domain to obtain the corrected estimate of the signal, $S_{S3\text{-}i}(t)$

The relevant calibration information is the correction function, which will be derived from calibration file parameters stored for each detector:

(i) nominal detector time constant, $\tau_{1\text{-}i}$
(ii) slow detector time constant, $\tau_{2\text{-}i}$
(iii) time constant amplitude factors, a_i.

The output of this module is a new set of timelines corresponding to the in-beam astronomical flux densities now corrected for the bolometer response: $S_{3\text{-}i}(t)$ for detector i.

It may be appropriate to leave this correction to the map-making stage. If that option is chosen, then this module can easily be by-passed or implemented such that no correction is actually done.

Implementaiton of this module is TBC (when it has been confirmed that there are no technical impediments and that the noise level is not degraded). The output timelines should contain the original timestamps with modified detector signal values attached.

The output of this module is a set of timelines of astronomical flux densities corrected for the bolometer time response: $S_{3\text{-}i}(t)$ for detector i.

5.8 Removal of optical crosstalk

Optical crosstalk is here defined as power from the astronomical sky that should be incident on one detector actually falling on another. It is important to note that in the case of SPIRE, neighbouring detectors are separated by an angle of $2\lambda/D$ on the sky, and even if a source is on-axis for a given pixel, some fraction of the source power will be incident on the neighbouring detectors due to telescope diffraction. Non-neighbouring detectors are sufficiently far apart that they should not pick up any power from an on-axis source.

Optical crosstalk can be characterised by a crosstalk matrix, $\mathbf{C_{opt}}$, analogous to the electrical crosstalk matrix described in Section 5.3. Let $\mathbf{S_3}$ be the input vector of flux densities for a given time step.

The vector of optical crosstalk-corrected flux densities is then given by

$$\mathbf{S}_4 = \mathbf{C}_{\mathbf{opt}}\,\mathbf{S}_3 \qquad (34)$$

As an illustration, if we had thee detectors, the matrix equation would be

$$\begin{bmatrix} S_{4\text{-}1} \\ S_{4\text{-}2} \\ S_{4\text{-}3} \end{bmatrix} = \begin{bmatrix} o_{11} & o_{21} & o_{31} \\ o_{12} & o_{22} & o_{32} \\ o_{13} & o_{23} & o_{33} \end{bmatrix} \begin{bmatrix} S_{3\text{-}1} \\ S_{3\text{-}2} \\ S_{3\text{-}3} \end{bmatrix} \quad (35)$$

Unlike the case of electrical crosstalk, the diagonal elements are not equal to unity since optical crosstalk involves loss of power from the primary detector.

The optical crosstalk matrix can be implemented as a calibration file. The values of o_{ij} must be determined from calibration observations involving scanning a strong point source across each of the detectors in the array.

In the absence of optical crosstalk, or if the crosstalk correction is to be left out, then the non-diagonal o_{ij} coefficients are set to zero and the diagonal coefficients are set to unity.

The output of this module is a set of flux density timelines: $S_{4\text{-}i}(t)$ for detector i, suitable for input to the map-making module.

5.9 Map-making

TBW based on Peirre Chanial's MadMap implementation.

- Instrument and housekeeping data that should be available in mapmaking to assist in possible further removal of correlations: telescope temperature, Level-1 temperature; ^{3}He temperature.

6. Point source and jiggle-map pipeline

6.1 Signals measured during chopping and nodding

There are some key differences between the pipelines for chopped photometric observation and scan map observations:

(i) for chopped observations, there is no need to correct for low-frequency noise associated with bath temperature fluctuations: it is assumed that such fluctuations are at frequencies lower than the chop frequency and so are chopped out;

(ii) in the case of chopped observations, the observation is inherently differential, and the calculated source flux density is measured with respect to the sky background in the vicinity of the source.

Due to small asymmetries in the optical system, the ambient background power in the two chop positions will be slightly different. The purpose of nodding is to subtract out this difference.

The principles of chopping and nodding are illustrated in Figure 22, where we assume that there is a source in the position that is common to both nod postions, and that the sky background varies with position.

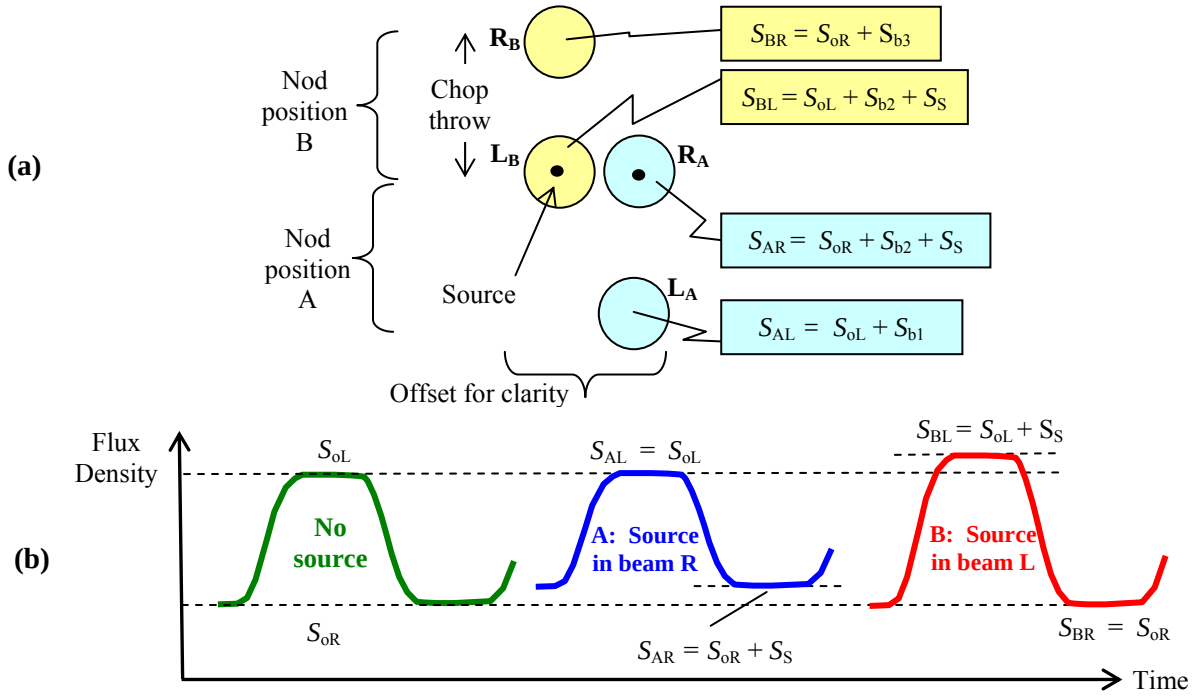

Figure 22: (a) Flux density levels measured during chopping and nodding L = left beam, R = Right beam) (b) Example timelines for nod positions A and B (with the source in the right beam for position A), where for simplicity the sky background is taken to be uniform.

Let S_{oR} and S_{oL} be the flux densities measured in the right and left beams for blank sky. Let S_{b1}, S_{b2} and S_{b3} be the sky background levels in the three positions, and let S_S be source flux density (i.e., the sky flux density at the position on the sky that is common to both nod cycles). The de-modulated chopped signal (R – L) for nod position A is $S_A = (S_{oR} + S_{b2} + S_S) - (S_{oL} + S_{b1})$, whilst that for position B is $S_B = (S_{oR} + S_{b3}) - (S_{oL} + S_{b2} + S_S)$. The difference (de-modulated nod signal) is this $S_A - S_B = 2S_S + (S_{b2} - S_{b1}) - (S_{b3} - S_{b2})$. Thus, if the sky background is uniform or varying linearly, it is removed. If there is a higher order variation in sky brightness, then it will not be completely subtracted.

The offset due to the asymmetric ambient background has thus been subtracted, and if the sky background is uniform or varying linearly, it is also removed. If there is a higher order variation in sky brightness, then it

will not be completely subtracted.

The above analysis is valid in the case of an observation of a particular sky position by a single detector. In tha case of point source observations, for a given array three detectors see the source at some time during the observation, as shown in Figure 23. The primary detector sees it in both nod cycles, as illustrated in Figure 22; however, the other two only see it in one of the nod positions.

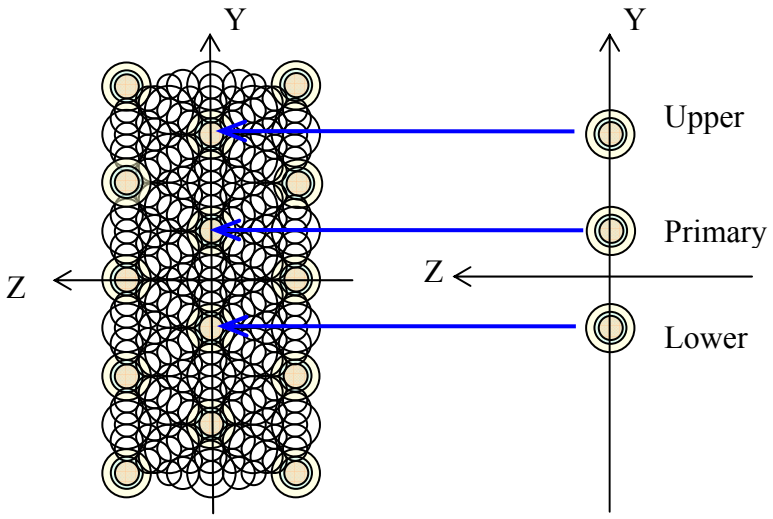

Figure 23: Nominal detector sets used for point source photometry.

In the couse of the observation, five different sky positions are viewed by the three detectors (per array). The corresponding signals are indicated in Figure 24, which also shows the positions viewed by the lower detector during the chopping and nodding cycles.

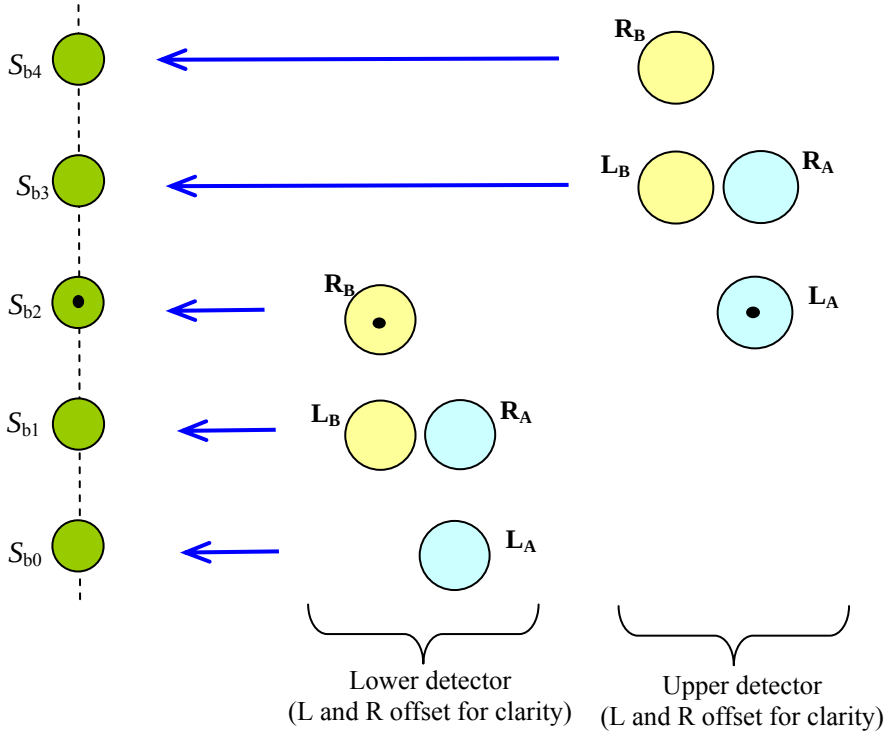

Figure 24: Five sky poistions viewed by the three detectors involved in point source photometry, and positions observed by the lower and upper detector set during chopping and nodding.

Let the sky background fux densty in the five positions be $S_{b0} - S_{b4}$, and let the source position coincide with S_{b2}. Then, for the lower detector we have:

Demodulated (R – L) signal for nod position A: $S_A = (S_{oR} + S_{b1}) - (S_{oL} + S_{b0})$
Demodulated (R – L) signal for nod position B: $S_B = (S_{oR} + S_{b2} + S_S) - (S_{oL} + S_{b1})$
Difference (de-nodded signel: $S_A - S_B = 2S_{b1} - (S_{bo} + S_{b2}) - S_S$

Similarly, for the upper detector we have:

Demodulated signal for nod position A: $S_A = (S_{oR} + S_{b3}) - (S_{oL} + S_{b2} + S_S)$
Demodulated signal for nod position B: $S_B = (S_{oR} + S_{b4}) - (S_{oL} + S_{b3})$
Difference (de-nodded signel: $S_A - S_B = 2S_{b3} - (S_{b4} + S_{b2}) - S_S$

If the sky background is uniform or linear, then $2S_{b1} = (S_{bo} + S_{b2})$ and $2S_{b3} - (S_{b4} + S_{b2})$, so we have

$$S_A = -S_S \quad \text{and} \quad S_B = -S_S. \tag{36}$$

We therefore get two additional estimates of the source signal, of half the magnitude as for the primary detector (but with the same noise level).

So the point source observation produces three separate estimates of the source flux density: $2S$ for the primary detector and S for each of the upper and lower detectors. Let the S/N for the central detector be σ, and assume that the three detectors have equal sensitivity. In that case the S/N for the upper and lower detectors is $\sigma/2$. If the three measurements are combined, the overall S/N is thus

$$\sigma_{tot} = \left[\sigma^2 + 2\left(\frac{\sigma}{2}\right)^2\right]^{1/2} = \left[\sqrt{\frac{3}{2}}\right]\sigma = (1.22)\sigma \tag{37}$$

The pipeline should calculate and quote the three estimates of the source flux density separately, and provide an option to combine them if the user so desired. Differences in the three measured values may be used to identify non-linear sky gradients.

6.2 Point source and jiggle map pipeline flow diagram

The SPIRE pipeline must operate over a wide range of source brightness, and the direct proportionality of voltage to flux density cannot be assumed. It is therefore necessary to carry out the demodulation process *after* conversion to flux density (see Section 6.5 below).

Figure 25 shows the sequence of steps in the point source and jiggle-map pipeline, and the individual modules are described in the subsections below.

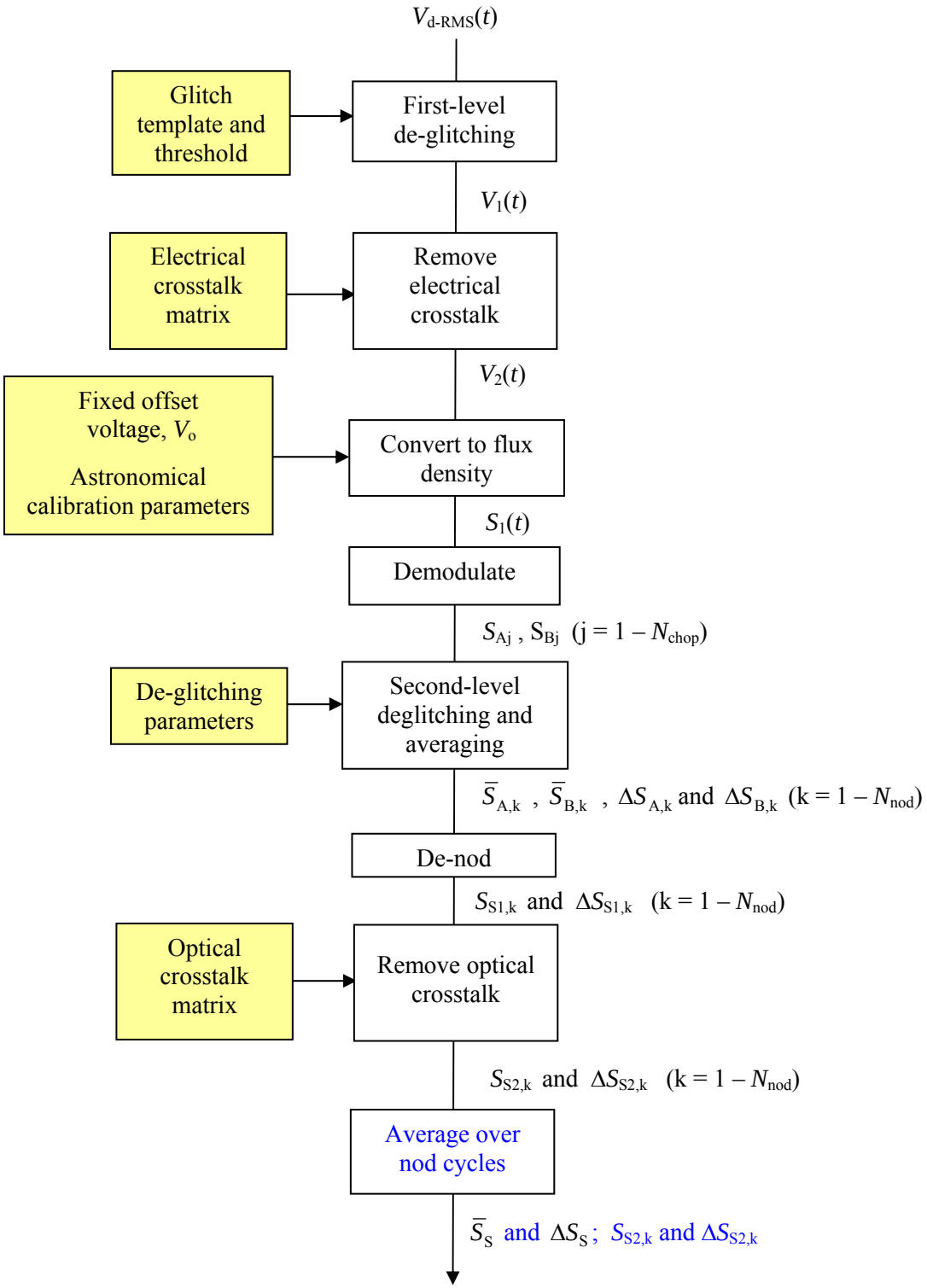

Figure 25: Pipeline block diagram for chopped/nodded observations (for one nod cycle at a single jiggle position with N_{chop} chop cycles per jiggle position).

6.3 First-level deglitching

As in the scan-map pipeline, before further processing of the measured detector voltage timeline, $V_{d\text{-}RMS}(t)$, glitches due to cosmic ray hits or other impulse-like events in the detectors will be removed. But the detector timelines in jiggle-map mode may legitimately contain large changes between contiguous samples in the case of chopping on a strong source.

The wavelet-based approach (Option 2 in Section 5.2) shall be adoptedas the baseline deglitching method. the simpler de-glitching scheme (Option 1) may be adopted for chopped modes.

The output of this module is the de-glitched voltage timeline, $V_{1\text{-}i}(t)$ for detector i.

6.4 Removal of electrical crosstalk

This module is the same as for the scan-map pipeline (Section 5.3). The output is the crosstalk-corrected voltage timeline, $V_{2\text{-}i}(t)$ for detector i.

6.5 Convert to flux density

The nominal method to be used to demodulate the chopped signal follows the logic outlined in Section 4.3. But because of the potentially non-linear relationship between voltage and flux density and voltage, it must be carried out in terms of flux density to ensure that the subtraction in the subsequent de-nodding step is done in the linear regime.

The voltage timelines $V_{2\text{-}i}(t)$ are converted to flux density timelines using the same module as for the scan-map pipeline (described in Section 5.5). The reference voltage V_o and the K-values are identical.

The output of this module is a set of flux density timelines: $S_{1\text{-}i}(t)$ for detector i.

6.6 Demodulate

Figure 26 shows example detector voltage timelines, as output by the previous module, corresponding to nod positions A and B (with the source in the right beam for position A), where for simplicity the sky background is taken to be uniform.

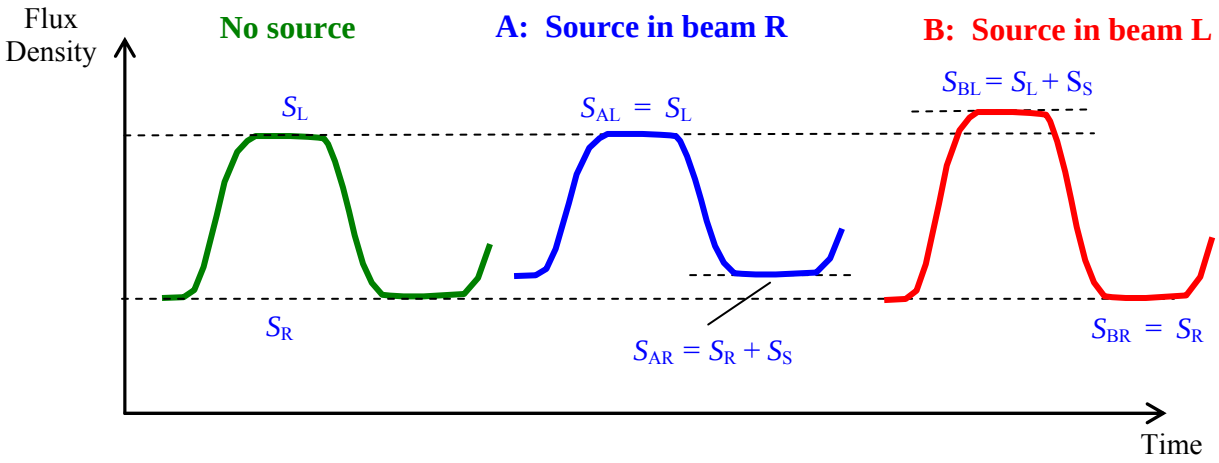

Figure 26: Example: chopped signal for nod positions A and B (assuming uniform sky background).

As drawn in Figure 26 , most of the difference between the chop positions is due to the asymmetric telescope background. In nod position A, the source increases the magnitude of the difference and in nod position B it decreases it.

The demodulated flux densities for nod positions A and B are calculated as follows:

$$S_A = \bar{S}_{AR} - \bar{S}_{AL} \qquad \text{and} \qquad S_B = \bar{S}_{BR} - \bar{S}_{BL} \tag{38}$$

where $\bar{S}_{AR}$, is the average of the three (TBC) samples the for the relevant half-cycle, as explained in Section 4.3, and similarly for the others.

Consider the demodulation for a given jiggle position with N_{chop} chop cycles per nod cycle and N_{nod} nod cycles. For each nod cycle, we have N_{chop} estimates of S_A and N_{chop} estimates of S_B.

As the output of this module, we then have, for each nod cycle, N_{chop} estimates of S_A and likewise N_{chop} estimates of S_B:

$S_{Aj,k}$ and $S_{Bj,k}$ where j = 1 – N_{chop} and k = 1 – N_{nod}.

Note that for most practical cases N_{nod} = 1, since the nominal jiggle map observation incorporates four nod cycles, each covering 16 different jiggle positions [3].

6.7 Second-level deglitching and averaging

For each nod cycle, the N_{chop} estimates of the demodulated flux densities in each of the two nod positions can now be deglitched by rejecting outliers and averaging the remaining samples, to produce mean values and an associated uncertainty.

The outputs of this module are, for each nod cycle, values of flux density and their associated uncertainties:

$$\bar{S}_{A,k} \;,\; \bar{S}_{B,k} \;,\; \Delta S_{A,k} \,,\; \Delta S_{B,k} \,.$$

6.8 De-nod

The de-nod process merely takes the difference between the flux densities in the two nod positions to derive the first estimate of the source flux density. For each of the N_{nod} nod cycles, we have:

$$S_{S1,k} = \frac{1}{2}\left(\bar{S}_{A,k} - \bar{S}_{B,k}\right) \qquad \text{with} \qquad \Delta S_{S1,k} = \left(\Delta S_{A,k}{}^2 + \Delta S_{B,k}{}^2\right)^{1/2} \quad . \tag{39}$$

The output of this module is a value of in-beam source flux density, $S_{S1,k}$, with an associated error $\Delta S_{S1,k}$, for each jiggle position of each detector, and for each of the k = 1 – N_{nod} nod cycles.

As noted in Section 6, if the sky background is uniform or varying linearly, it is also removed; but if there is a higher order variation in sky brightness, then it will not be completely subtracted.

6.9 Removal of optical crosstalk

Optical crosstalk is removed using the same method described in Section 5.8. The output of this module is then, for each jiggle position of each detector, and for each nod cycle, an estimate, $S_{S2,k}$, of the in-beam source flux density and its associated statistical uncertainty, $\Delta S_{S2,k}$.

Note that the crosstalk matrix elements may be different to those in the case of the scan map pipeline (Section 5.8) due to the different BSM positions.

6.10 Average over nod cycles

If N_{nod} > 1, then a weighted mean and uncertainty can be calculated from the separate estimates:

$$\bar{S}_S = \frac{\sum_{k=0}^{N_{nod}} \frac{S_{S2,k}}{\Delta S_{S2,k}}}{\sum_{k=0}^{N_{nod}} \frac{1}{\Delta S_{S2,k}}} \quad \text{and} \quad \Delta S_S = \left[\frac{1}{\sum_{k=0}^{N_{nod}} \left(\frac{1}{\Delta S_{S2,k}} \right)^2} \right]^{1/2} . \tag{40}$$

Note: a weighted mean is only legitimate if the individual values and their uncertainties are mutually compatible. In order to avoid vulnerability to any anomalous estimates and to provide a means of identifying any such anomalies, the pipeline should therefore preserve and continue to process the results of the individual nod cycles in addition to the averaged result.

The outputs of this module are therefore, for each jiggle position of each detector,

(i) the weighted average flux density $\bar{S}_S$ and its associated uncertainty ΔS_S;
(ii) for each individual nod cycle: $S_{S2,k}$ and $\Delta S_{S2,k}$ (i.e., just the inputs).

6.11 Calculation of point source flux density and positional offset (point source photometry only)

As noted in Section 6.1, in a point source observation, three detectors on a given array provide a measurement of the source (primary, upper, and lower). Consider any one of the measurements. It will involve observations of seven BSM offset positions, with the central (0,0) position observed twice. For each of the eight positions we have a flux density estimate and its statistical uncertainty, $S_i \pm \Delta S_i$, and an angular offset on the sky with respect to the nominal (0,0) pointed position, ($\Delta\theta_{yi}$, $\Delta\theta_{zi}$).

The pipeline assumes that the source is point-like and carries out a weighted fit of the eight points to a 2-D Gaussian representation of the beam profile. The free parameters for the fit are the peak flux density and the Y and Z positional offsets with respect to the central position (0,0). The results are fitted flux density and offsets, and their associated uncertainties. The estimation of flux density and postion are carried out independently

- for each of the N_{nod} nod cycles
- for each of the three detectors (primary, upper and lower) on each array.

All of these measurements are also combined together by taking a weighted mean.

Note that:

(i) The quality of the positional offset fit will be highly sensitive to S/N. As a rule of thumb, the S/N on the position fit is roughly equivelaent to the S/N on the peak position (so for instance, a S/N of about 20 for PSW should result in an uncertainty of ~ 1" in position since the beam FWHM is close to 20"). For low S/N observations, the position fit will not be reliable. The adopted routine must therefore produce an indication of the reliability of the fit.
(ii) In the case of low-S/N data, the fitted flux density should be essentially equivalent to the weighted sum of the eight measured points (i.e., weighted with respect to the relative beam profile response in the different positions, under the assumption of accurate pointing).

7. Astronomical calibration

7.1 Determination of the voltage-flux density conversion constants

Consider first the small-signal regime in which the signal voltage, V_S (= $V_3 - V_o$) is directly proportional to flux density (i.e., only the K_1 term in equation 33 is significant):

$$S = K_1(V_3 - V_o) = K_1 V_S . \tag{41}$$

K_1 has units Jy V^{-1}.

Let $S_S(\nu)$ be the in-beam flux density of the source at the telescope aperture.

V_S is given by

$$V_S = UQ_S = UA_{Tel} \int_{Passband} S_S(\nu)\eta(\nu)\, d\nu , \tag{42}$$

where A_{Tel} is the effective telescope area and $\eta(\nu)$ is a function representing the overall combination of various efficiencies in the telescope and instrument (obscuration, filters, optics, detector absorption, etc.). If we normalise the product of responsivity, telescope area and $\eta(\nu)$ in terms of the relative spectral response function (RSRF), $R(\nu)$ and some calibration constant B, such that

$$U\, A_{Tel}\, \eta(\nu) = \frac{R(\nu)}{B} , \tag{43}$$

then

$$V_S = \frac{1}{B} \int_{Passband} S_S(\nu) R(\nu)\, d\nu . \tag{44}$$

The automatic pipeline must make no assumptions concerning the source spectrum – this is something to be decided upon by the observer, or derived subsequently from a multi-wavelength data-set (SPIRE only or SPIRE plus other measurements such as PACS and/or ground-based observations). Therefore at this stage we must assume a standard spectral form for the source. The simplest approach is to assume that the spectrum is a power law across the band defined by an index α_S:

$$S_S(\nu) = S_S(\nu_o)\left(\frac{\nu}{\nu_o}\right)^{\alpha_S} , \tag{45}$$

where we can choose ν_o to be some suitable frequency within the band - for instance at or near the band centres (250, 350, 500 μm) for the three photometer bands.

Typical values for α_S would be 2 for a black body in the Rayleigh-Jeans region, 3 - 4 for a dust source in the Rayleigh-Jeans region, or close to 0 for a flat-spectrum radio source or a thermal source observed near the peak of its Spectral Energy Distribution (SED). A wide range of values of α can therefore be expected for SPIRE observations of various kinds.

The signal voltage is then

$$V_S = \frac{S_S(\nu_o)}{B\nu_o^{\alpha_S}} \int_{Passband} R(\nu)\nu^{\alpha_S}\, d\nu , \tag{46}$$

and the source flux density at frequency ν_o is

$$S_S(\nu_o) = \left(\frac{B \nu_o^{\alpha_S}}{\int_{Passband} R(\nu) \nu^{\alpha_S} \, d\nu} \right) V_S = K_1 V_S . \quad (47)$$

K_1 incorporates many factors and is difficult to determine except by observation of a standard astronomical source. Assume that we have such a calibrator with a known spectrum given by

$$S_C(\nu) = S_C(\nu_o) \left(\frac{\nu}{\nu_o} \right)^{\alpha_C} . \quad (48)$$

For an observation of the calibrator yielding signal voltage V_C, we have

$$S_C(\nu_o) = \left(\frac{B \nu_o^{\alpha_C}}{\int_{Passband} R(\nu) \nu^{\alpha_C} \, d\nu} \right) V_C , \quad (49)$$

from which we can calculate B:

$$B = \frac{S_C(\nu_o) \int_{Passband} R(\nu) \nu^{\alpha_C} \, d\nu}{V_C \nu_o^{\alpha_C}} , \quad (50)$$

and K_1 :

$$K_1 = \frac{S_C(\nu_o)}{V_C} \left[\frac{\nu_o^{\alpha S}}{\nu_o^{\alpha_C}} \right] \left[\frac{\int_{Passband} R(\nu) \nu^{\alpha_C} \, d\nu}{\int_{Passband} R(\nu) \nu^{\alpha_S} \, d\nu} \right] . \quad (51)$$

Flat fielding for mapping observations is accomplished by establishing the value of K_1 for each detector in an array. Note that manner in which the normalisation of the RSRF is done is not critical – it could be done by setting either the peak or the area equal to unity – this would result in different values of B being derived, but the same value for K_1 . For SPIRE it will be normalised such that the peak value is unity.

Note that in the idealised case of a top-hat filter and $\alpha_C = 0$, we would have $B = \frac{S_C(\nu_o) \Delta \nu}{V_C}$.

We can now derive $S_S(\nu_o)$ from an observation of V_S and an assumed value of α_S. For this we need to know the integrals $\int_{Passband} R(\nu) \nu^{\alpha_C} \, d\nu$ and $\int_{Passband} R(\nu) \nu^{\alpha S} \, d\nu$ (in the form of calibration files).

Note that accurate knowledge of this integral is not actually critical to the calibration unless the source and calibrator spectral indices are very different, as it tends to ratio out in equation (49):

$$K_1 \approx \frac{S_C(\nu_o)}{V_C} \qquad \text{if } \alpha_C \approx \alpha_S \,. \tag{52}$$

So if the source and calibrator have the same spectral index ($\alpha_S = \alpha_C$), then the expression for the source flux density reduces to a simple ratio as we would expect:

$$S_S(\nu_o) = S_C(\nu_o)\left[\frac{V_S}{V_C}\right] = K_1 V_S \,. \tag{53}$$

Because the pipeline processing cannot pre-judge the source spectrum, we must assume a nominal value, $\alpha_S = \alpha_{nom}$ and quote the corresponding flux densities. The observer can then re-calibrate the corresponding flux densities to some other value of α_S if desired.

The convention to be used for SPIRE and PACS is $\alpha_{nom} = -1$, corresponding to νS_ν flat across the band. It is still possible to derive B from observations of a calibrator with a different spectrum, as long as we know what it is (most of our calibrators are likely to have black or near-black body spectra within a band, for which $\alpha_C = 2$).

Equation (45) then becomes

$$S_S(\nu_o) = \frac{BV_S}{\nu_o \int_{Passband} \frac{R(\nu)}{\nu}\, d\nu} = K_1 V_S \,. \tag{54}$$

In the simple case of a top-hat filter, this would be $S_S(\nu_o) = \left[\frac{B}{\nu_o \ln\left(\frac{\nu_2}{\nu_1}\right)}\right] V_S$.

7.2 Conversion of measured flux densities to a different source spectral index (colour correction)

As discussed above, all results will be calculated and quoted under the assumption that the source has a spectrum with νS_ν flat across the band ($\alpha_{Snom} = -1$). This will not be the case for most observations, and a correction will need to be applied by the astronomer based on other information (for instance, measurements in other SPIRE or PACS bands and/or data from other telescopes).

Again, let us assume that the source spectrum actually follows a power law with a different index α_S. Let $S'_S(\nu_o)$ be the source flux density at ν_o for that spectral shape. We then have from equation (45),

$$\frac{S'_S(\nu_o)}{S_S(\nu_o)} = \nu_o^{(\alpha_S - \alpha_{nom})} \left[\frac{\int_{Passband} R(\nu)\nu^{\alpha_{nom}}\, d\nu}{\int_{Passband} R(\nu)\nu^{\alpha_S}\, d\nu}\right] . \tag{55}$$

The factor in brackets can easily be computed and tabulated for various values of α_S, so that the astronomer can implement a straightforward multiplicative correction factor corresponding to the chosen spectral index. Figure 27 shows the correction factor vs. adopted source spectral index for the currently assumed photometer filter profiles, taking α_{nom} = -1 (the filter profiles will be updated in the near future, but not such as to change these curves significantly). Typical SPIRE sources will have α in the range 0 – 3, requiring corrections up to a few %.

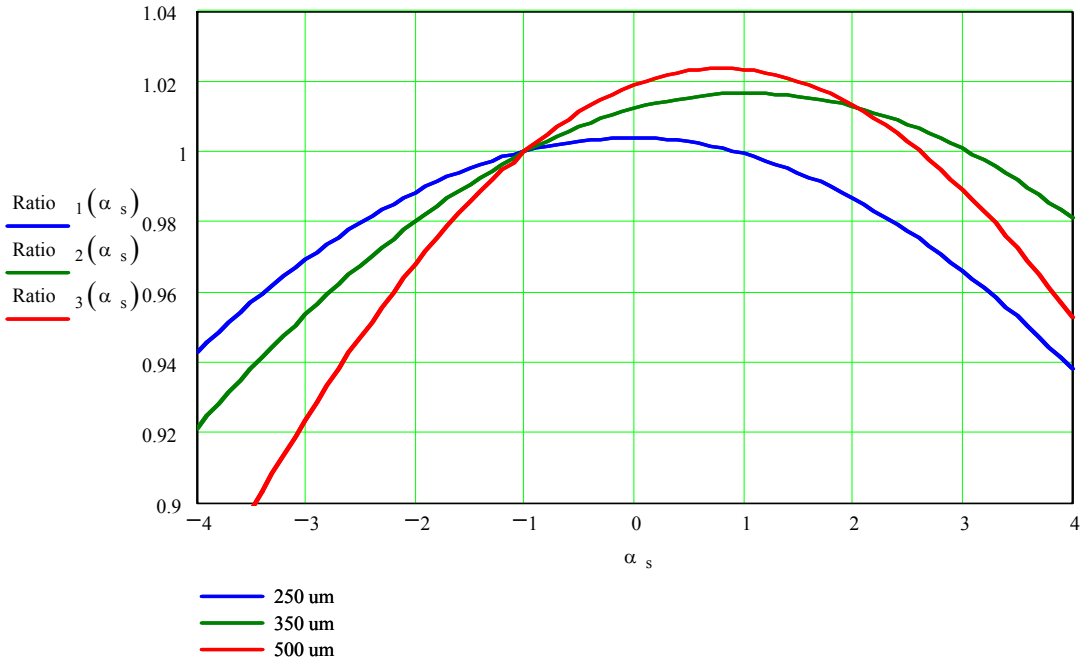

Figure 27: Spectral index correction factor vs. true source spectral index for the currently assumed SPIRE filter bands and $\alpha_{nom} = -1$.

Note that it is equally straightforward to convert the results to some other wavelength if that is desired. Sometimes it is the practice to quote the measured flux density at a flux-weighted effective wavelength, to take into account the fact that the measurement is biased towards one side of the band in the case of a source with a steep spectrum. We propose not to adopt this practice here for two reasons:

(i) it is no more accurate or correct than the scheme described above;
(ii) we can avoid complication and potential confusion by selecting a standard set of wavelengths for all measurements.

8. References

1 *DCU Design Document*, SA-SPIRE-FP-0063-02, Issue 1.0, 11 July 2005.
2 *SPIRE Spectrometer Pipeline Description*, SPIRE-BSS-DOC-002966, Version 1.5, 2 October 2007.
3 *Operating Modes for the SPIRE Instrument* SPIRE-RAL-DOC-000320, Issue 3.3, 24 June 2005.
4 *SPIRE Design Description*, SPIRE-RAL-PRJ-000620, Issue 1.0, February 2002.
5 *Sensitivity of the SPIRE Detectors to Operating Parameters*, SPIRE-UCF-DOC-002901, November 14 2007.